coatings

MDPI

Review

Interfacial Bonding and Residual Stress of Single Splats on Solid Substrates: A Literature Review

Chao Kang [1] and Motoki Sakaguchi [2,*]

[1] College of Mechanical Engineering, Zhejiang University of Technology, No. 288 Liuhe Road, Xihu District, Hangzhou 310023, China; kangchao@zjut.edu.cn
[2] Department of Mechanical Engineering, Institute of Science Tokyo, O-Okayama 2-12-1, Meguro-ku, Tokyo 152-8552, Japan
* Correspondence: sakaguchi.m.cc77@m.isct.ac.jp

Abstract

The impingement of a molten droplet on a solid surface, forming a "splat," is a fundamental phenomenon observed across numerous industrial surface engineering techniques. For example, thermal spray deposition is widely used to create metal, ceramic, polymer, and composite coatings that are vital for aerospace, biomedical, electronics, and energy applications. Significant progress has been made in understanding droplet impact behavior, largely driven by advancements in high-resolution and high-speed imaging techniques, as well as computational resources. Although droplet impact dynamics, splat morphology, and interfacial bonding mechanisms have been extensively reviewed, a comprehensive overview of the mechanical behaviors of single splats, which are crucial for coating performance, has not been reported. This review bridges that gap by offering an in-depth analysis of bonding strength and residual stress in single splats. The various experimental techniques used to characterize these properties are thoroughly discussed, and a detailed review of the analytical models and numerical simulations developed to predict and understand residual stress evolution is provided. Notably, the complex interplay between bonding strength and residual stress is then discussed, examining how these two critical mechanical attributes are interrelated and mutually influence each other. Subsequently, effective strategies for improving interfacial bonding are explored, and key factors that influence residual stress are identified. Furthermore, the fundamental roles of splat flattening and formation dynamics in determining the final mechanical properties are critically examined, highlighting the challenges in integrating fluid dynamics with mechanical analysis. Thermal spraying serves as the primary context, but other relevant applications are briefly considered. Cold spray splats are excluded because of their distinct bonding and stress generation mechanisms. Finally, promising future research directions are outlined to advance the understanding and control of the mechanical properties in single splats, ultimately supporting the development of more robust and reliable coating technologies.

Keywords: splat deposition; thermal spray; bonding strength; residual stress; individual particle

check for updates

Academic Editor: Alessandro Patelli

Received: 10 September 2025
Revised: 7 October 2025
Accepted: 28 October 2025
Published: 31 October 2025

Citation: Kang, C.; Sakaguchi, M. Interfacial Bonding and Residual Stress of Single Splats on Solid Substrates: A Literature Review. *Coatings* **2025**, *15*, 1259. https://doi.org/10.3390/coatings15111259

Copyright: © 2025 by the authors. Licensee MDPI, Basel, Switzerland. This article is an open access article distributed under the terms and conditions of the Creative Commons Attribution (CC BY) license (https://creativecommons.org/licenses/by/4.0/).

1. Introduction

1.1. Background

The impingement of droplets on solid surfaces is a fundamental phenomenon with broad relevance across numerous industrial and scientific domains. Specifically, in processes like thermal spraying, molten or semi-molten particles impact a substrate and

undergo rapid solidification, leading to the formation of pancake-shaped structures known as "splats" [1]. Each splat serves as the foundational building block for creating a protective or functional layer. These splats, composed of metals [2], ceramics [3], polymers [4], or composites [5], are widely used in aerospace components [6], biomedical implants [7], electronics [8], and energy systems [9].

Among the industrial deposition techniques, thermal spraying, which encompasses plasma spraying [10], flame spraying [11], and high-velocity oxy-fuel spraying [12], is particularly advantageous owing to its low cost and the ease of depositing thick coatings using a wide range of materials. Distinct from cold spray processes [13,14], where bonding is predominantly achieved through plastic deformation without particle preheating, thermal spraying involves rapid melting and solidification. This unique characteristic gives rise to distinct interfacial bonding phenomena and complex stress evolution that critically affect overall coating performance. Despite the extensive literature on droplet impact dynamics, the mechanical behaviors at the single splat scale, specifically those concerning interfacial bonding strength and residual stress, remain relatively underexplored.

Given the significant influence of drop impact phenomena, previous reviews have comprehensively addressed various factors associated with this complex process. These include the intrinsic aspects of fluid flow [15–17], the dynamics of splat solidification [18,19], the distribution of impact forces and stresses [20], and the broader mechanics of splat formation [1,21–24] and interfacial bonding [25]. Furthermore, reviews have delved into specific applications, such as spray cooling [26], water droplet freezing [27], heterogeneous droplet behavior [28], interactions with hot walls [29], superhydrophobic surfaces [30], and the behavior of complex fluids [31].

These works provide invaluable insights into fluid dynamics and solidification, but they often neglect the subsequent mechanical behavior of individual splats. Moreover, they rarely detail how bonding strength is formed, measured, and influenced by process parameters, and they do not extensively cover how residual stresses evolve and contribute to critical issues like delamination, cracking, and eventual coating failure. This research gap underscores a critical disconnect between the initial fluid dynamics and solidification of splats and the ultimate performance of coatings. Coating performance, particularly its durability and integrity, is fundamentally governed by the mechanical properties derived during deposition and solidification. This gap hinders the rational design of thermal spray processes for specific application requirements because the links between process parameters (fluid dynamics) and final coating reliability (mechanical properties) have not been fully elucidated. This review directly addresses these issues and bridges the gap by uniquely focusing on the mechanical consequences of splat formation, especially the fundamental aspects of bonding mechanisms and residual stress development. While previous reviews often focus on overall coating properties or specific phenomena like fluid dynamics, our novelty lies in the integrated and critical examination of how the transient dynamics of a single splat affect the critical mechanical outputs.

1.2. Interfacial Bonding and Residual Stress of Single Splats

Generally, three primary mechanisms contribute to splat adhesion: physical bonding, mechanical interlocking, and chemical bonding [3]. Physical bonds, often referred to as Van der Waals forces, represent a relatively weak form of interfacial connection [32]. In contrast, mechanical interlocking and chemical bonding are considerably more robust and are the principal targets for enhancing interfacial bonding strength. Chemical bonding is particularly difficult to achieve in thermal spraying, primarily owing to the rapid solidification rates and inherently limited diffusion time [33]. The bonding characteristics of single splats are typically assessed by evaluating their tensile and shear strength, which correspond to the

mode I (opening) and mode II (sliding) fractures, respectively. Although several experimental methods have been developed to quantify the bonding strength of single splats over the past couple decades, directly measuring this strength remains a significant challenge.

Residual stress in deposited splats originates from three main phenomena, namely high-velocity impact, rapid cooling contraction, and thermal mismatch, which induce peening stress, quenching stress, and thermal stress, respectively. Peening stress, inherently compressive, results from plastic deformation and serves as the dominant contributor to the residual stress in cold spraying [13]. Quenching stress, conversely, develops as the splat cools from its stress-free temperature to the substrate's temperature [34]. Thermal stress subsequently emerges during the further cooling of both the splat and the substrate down to ambient temperatures, and the tensile or compressive character depends on the thermal mismatch between splats and substrates. Several factors contribute to the relaxation of these residual stresses, including microcracking, viscous deformation, interfacial defects, and interfacial sliding [34]. Despite ongoing efforts, developing a precise numerical or theoretical model for predicting residual stress in single splats remains a significant challenge.

Furthermore, residual stress affects bonding strength measurements [35–37], yet the exact mathematical correlation and underlying mechanisms between these two properties remain largely unknown, warranting further investigation. It is important to note an asymmetry in the current research landscape regarding these two properties. The experimental characterization of interfacial bonding strength has been widely reported in previous studies, whereas the theoretical and numerical analyses are comparatively limited. In contrast, for residual stress, analytical models and numerical simulations aimed at elucidating its complex generation mechanisms and enabling prediction have been actively pursued.

The mechanical behaviors of deposited splats, encompassing both bonding strength and residual stress, are intrinsically influenced by the flattening and solidification processes. These processes, in turn, are dictated by the deposition conditions, such as the particle's initial temperature, impact velocity, and the substrate's preheating temperature [38–40]. To fully comprehend the stress generation and bonding mechanisms, the priority is to understand the fundamental splat formation mechanisms and their subsequent effects on mechanical properties. The transient solidification that occurs immediately after impact plays a pivotal role, directly influencing the subsequent stress generation process, and thus remains a major focus within drop impact studies. In thermal spraying, the particle is typically molten or semi-molten, meaning the dynamics are governed by fluid mechanics, rapid heat transfer, and subsequent rapid solidification, all of which occur within microseconds. Crucially, this transient solidification process is the primary determinant of both interfacial contact quality and the initial non-uniform temperature field that seeds quenching stress.

1.3. Structure of This Review

This review is structured to provide a comprehensive analysis of the mechanical properties of single splats. This paper is structured as follows:

Section 2 provides a comprehensive overview of the experimental methods specifically designed for evaluating the bonding strength of individual splats, considering both direct and indirect testing techniques.

Section 3 discusses the experimental approaches used to characterize residual stress at the splat level, including methods like curvature measurement, nano-indentation, and advanced microscopy.

Section 4 covers the analytical and numerical models developed for calculating and predicting residual stresses.

Section 5 delves into the complex interrelationship between bonding strength and residual stress, exploring strategies for improving interfacial bonding and identifying

key factors that influence residual stress. The fundamental role of splat dynamics in determining these mechanical properties is also discussed.

Finally, Section 6 summarizes the main findings and provides insights into future research directions within this specialized field.

The structure of this review, by systematically progressing from fluid dynamics (Section 5.1), through thermal events (Section 5.3), and culminating in the mechanical outcomes (Sections 2 and 3), is specifically designed to elucidate these links between the initial process parameters and the final mechanical properties.

2. Testing Methods of the Bonding Strength in Single Splats

This section thoroughly reviews the various experimental techniques employed to quantify the bonding strength of individual splats, discussing their principles, applications, and limitations.

The assessment of bonding strength must be coupled with an understanding of the dominant failure mechanisms and their underlying fracture mechanics. In single splats, failure occurs through three primary pathways: interfacial debonding (adhesive failure), cohesive failure (fracture within the splat or substrate), or interfacial sliding (failure under shear or mixed-mode loading). Delamination typically propagates under mixed-mode conditions. Fracture mechanics characterizes this failure based on the crack opening modes: Mode I (opening, tensile stress perpendicular to the interface), Mode II (in-plane shear/sliding), and Mode III (anti-plane shear/tearing). Residual stresses dramatically influence failure by altering the local mode mixity near a crack tip.

Splat–substrate adhesion is fundamentally governed by splat formation. Key factors influencing the adhesion mechanism include the temperature of substrate, the energy of sprayed particles, and surface properties [41–46]. Commonly employed approaches for evaluating the interfacial adhesion strength of thermal spray coatings include the scratch test [47], tensile test [48], indentation test [49], bending test [50], and scraping test [51]. However, because of their microscale features and irregular geometry, fewer methods and results have been published regarding the bonding strength of individual deposited splats. Table 1 summarizes the experimental techniques for measuring the bonding strength of single splats. The details of each method are reviewed in the following subsections.

2.1. Tensile Test

The tensile bonding strength of a paraffin wax splat deposited on polymer substrates was examined using a simple pull-off method [52]. This study examined the impact of a 3.1 mm paraffin wax droplet, which was released from heights of 20–50 mm onto Teflon and porous polyethylene surfaces. The components of the testing system are shown in Figure 1a–d, where a cylinder was used to bond the splat surface with a structural epoxy. Pores with diameters of 35 or 70 μm were introduced in the substrate to examine the effect of surface penetration, and the bonding strength was evaluated using an analytical model:

$$F = \sigma A_r + \varepsilon A_c \quad (1)$$

Here, A_r and A_c represent the cross-sectional area of the splat material within the holes and the contact area between the splat and the substrate, respectively. The experimentally determined σ and ε values denote the tensile strength of the splat and the adhesive force per unit area, respectively. The reliability of this equation was verified by comparing the calculated results with the experimental results. As shown in Figure 1e, the measured maximum forces were comparable to the predicted forces for both pore sizes across various droplet release heights.

Table 1. Summary of the experimental techniques used to determine bonding strength.

Splat Material	Substrate Material	Method	Bonding Strength [MPa]	Reference
Wax	Teflon, polyethylene	Tensile	0.1–0.2	[52]
Thermoplastic matrix	Carbon fibers	Scraping	5–10	[53]
Epoxy resin	Single carbon fiber	Scraping	30–80	[54]
ZrO_2-8 wt.%Y_2O_3	CoNiCrAlY bond coat + nickel-base superalloy	Scraping	7–13	[55]
Wax	430 stainless steel	Scraping	2–5	[56]
ZrO_2-8 wt.%Y_2O_3	Stainless steel	Scraping	100–400	[57]
Al_2O_3	Stainless steel 304	Indentation	70–140 (strain energy release rate [J/m^{-2}])	[58]
CoNiCrAlY	Ni-based superalloy	FIB-milled microcantilever beam bending	0–2500	[59]
Al_2O_3	Ni-based superalloy	Scratch	–	[60]
Al_2O_3, Al_2O_3-4 wt.%CNT, Al_2O_3-8 wt.%CNT	Steel	Scratch	0.5–7.4	[61]
Al_2O_3, TiO_2	C20 steel	Scratch	–	[62]
Carbon nanofiller-reinforced Al_2O_3	AISI 1020 steel	Scratch	0.2–1.1	[63]
Fe-based amorphous alloy	AISI 1045 steel	Scratch	7–18	[64]

FIB, focused ion beam.

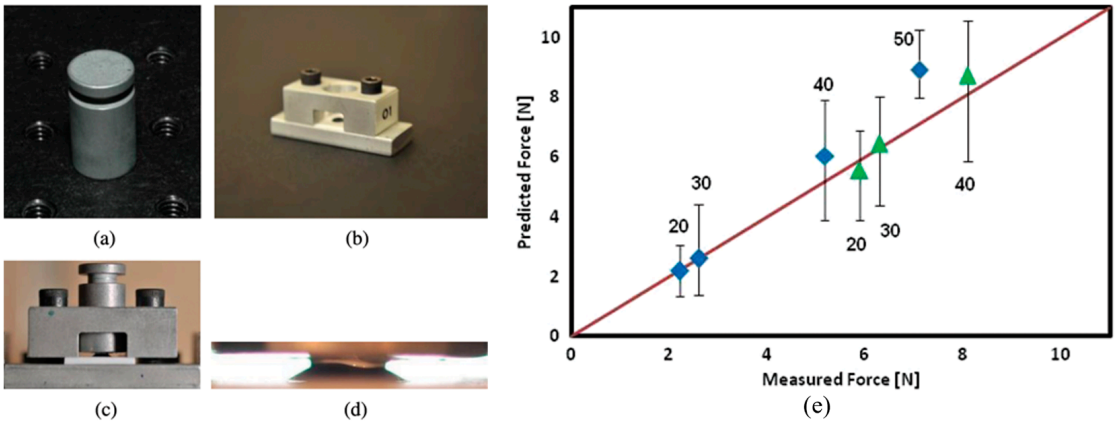

Figure 1. (**a**) Cylinder used for splat removal. (**b**) Sample holder. (**c**) Cylinder attached to the splat with epoxy. (**d**) Enlarged view of the attachment. (**e**) Comparison of the predicted maximum pull-off forces with those measured on porous polyethylene surfaces (blue diamonds, 35 µm pores; green triangles, 70 µm pores). The numbers (20, 30, 40, and 50) indicate the droplet release heights in millimeters [52].

2.2. Scraping Test

The scraping test is another method used to measure interfacial shear strength [53–57]. Kang et al. used a cutting blade coupled with a load cell to push a paraffin wax splat away from the substrate along the splat/substrate interface. The force evolution was recorded as a function of the blade's moving distance [56]. The results are shown in Figure 2a–d, illustrating the effects of various splat deposition conditions, including (a) substrate temperature (T_{sub}),

(b) free-fall height (H), which relates to impact velocity, and droplet temperature (T_{drop}) with (c) low and (d) high residual stress in the splats. Bonding strength was quantified using the parameter $K(d)$:

$$K(d) = {}^{F(d)} \Big/ b(d) \cdot t(d) \quad (2)$$

$K(d)$ is derived as a function of displacement (d) using the real-time scraping force ($F(d)$), splat thickness ($t(d)$), and scraping breadth ($b(d)$). Both $b(d)$ and $t(d)$ are obtained from the recorded splat profiles and force–displacement plots. With the splat diameter held at approximately 10 mm, the interfacial adhesion strength was quantified using K_0. This value is simply $K(d)$ measured at the maximum applied force (F_{max}), which was reliably observed at a displacement between 2 and 7 mm. F_{max} and the calculated K_0 for each deposition condition are plotted in Figure 2e–h. The scraping test demonstrated good repeatability, as confirmed by the coefficient of variation for K_0 being consistently less than 8% across all fixed substrate temperatures and impact conditions tested. The minor scatter observed in the K_0 values, despite the low coefficient of variation, is primarily attributed to experimental variations. These contributors to the scatter include splat-to-splat variation in geometry, minor misalignments of the scraper blade, and inherent variations in the prior residual stress state within the splat prior to scraping. The results also indicate that interfacial bonding strength was significantly influenced by the deposition conditions, with superior adhesion achieved at higher substrate preheating temperatures, greater drop heights, and higher droplet temperatures. The scraping test results were compared with residual stress-induced interfacial debonding and numerically calculated stress distributions along the interface. The scraping test findings were mutually consistent with the numerical results and observed debonding phenomena.

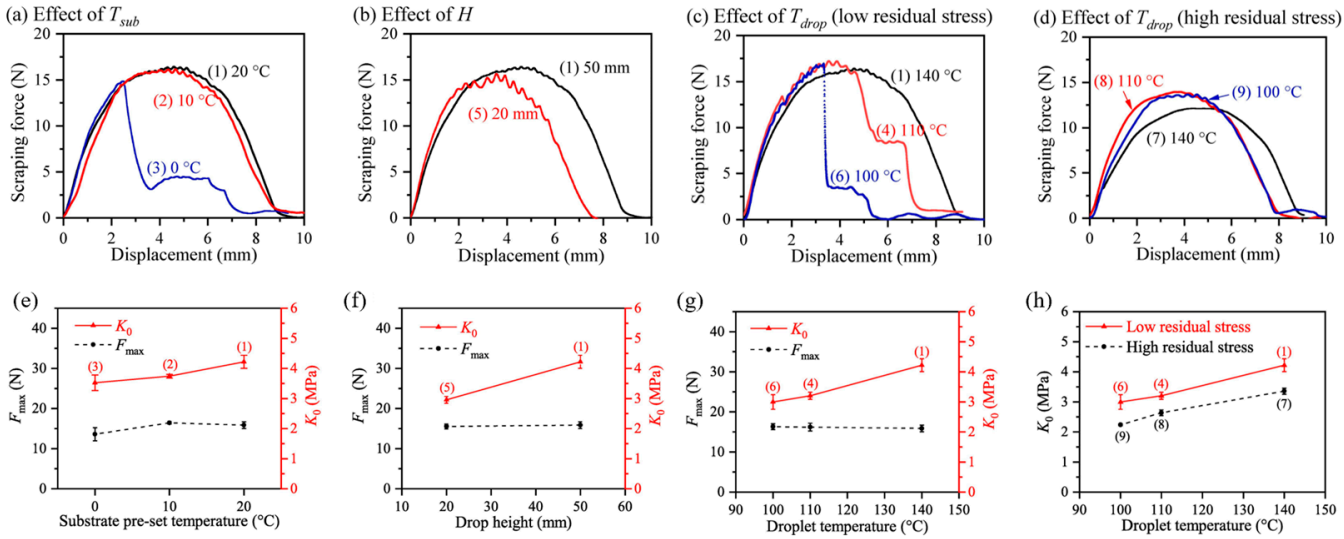

Figure 2. (**a**–**d**) Force vs. displacement data recorded during scraping a paraffin wax splat from a metallic substrate. The plot investigates the influences of (**a**) temperature of substrate (T_{sub}), (**b**) free-fall height (H) which relates to impact velocity, and (**c**) temperature of the droplet (T_{drop}) with low and (**d**) high residual stress, where the residual stress is controlled by creep-induced stress relaxation. (**e**–**g**) The effects of (**e**) substrate pre-set temperature, (**f**) drop height, and (**g**) droplet temperature on F_{max} and K_0. (**h**) The effects of droplet temperature and residual stress on K_0 [56].

A more recent study employed a scraping test to examine the micro-shear strength of a ceramic splat deposited on a metal substrate at supersonic or subsonic velocities, investigating the effect of splat morphology [57]. This study revealed that the micro-adhesive properties of needle-shaped splats were enhanced by the interlocking of submicron/nano-

columnar grains and restructured amorphous phases. For splashing splats, the adhesion force was observed to be twice as high in the central region as in the periphery. This significant difference is primarily attributed to the air film beneath the peripheral area [65].

2.3. Indentation Test

The indentation method was used by Balić et al. to investigate the bonding strength of single splats (Figure 3) [58]. The strain energy release rate of alumina (Al_2O_3) splats deposited on stainless steel 304 substrates was characterized by directly observing interfacial crack propagation during indentation:

$$G = \left(1 - \nu^2\right) t\sigma_0^2 / 2E \tag{3}$$

Here, E is the splat's Young's modulus, ν represents the splat's Poisson's ratio, and t is splat thickness. σ_0 is the indentation stress, defined as the compressive stress generated in the region above the prospective crack. This stress directly accounts for the material's reaction to the volume of deformation caused by the indentation:

$$\sigma_0 = \frac{EV_0}{2\pi(1-\nu)a^2 t} \tag{4}$$

where $2a$ is prospective crack length. V_0 is indentation volume in splat, derivable from the depth of indentation and geometry of indenter tip. Crack length was determined by measuring the radial distance from the indentation axis to the edge of the splat that first exhibited debonding. Consequently, G can be re-expressed by substituting Equation (4) into Equation (3):

$$G = \frac{\left(1 - \nu^2\right) t\left(\frac{EV_0}{2\pi(1-\nu)a^2 t}\right)^2}{2E} \tag{5}$$

The calculated G values were comparable with those for similar bi-material combinations, specifically the interfacial fracture energy of oxide/metal (Al_2O_3/Au) interfaces [66]. A significant limitation preventing the widespread application of this method is the need to simultaneously perform the test and scanning electron microscopy (SEM) to capture in situ images during indentation for accurate crack length determination.

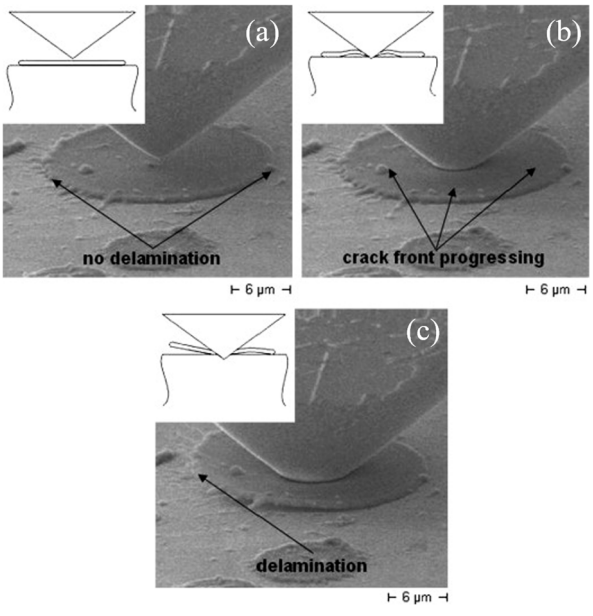

Figure 3. Secondary electron images obtained during nano-indentation of alumina splats deposited on stainless steel 304 substrates: (**a**) pre-indentation, (**b**) during indentation, and (**c**) post-indentation [58].

2.4. Focused Ion Beam-Milled Microcantilever Beam Bending Test

Fanicchia et al. carried out beam bending tests on focused ion beam (FIB)-milled microcantilevers for investigating the micro bonding strength of a single splat [59]. Fracture strength was measured at various locations along the interface between splat and substrate employing an in situ SEM indenter. Figure 4a presents an SEM micrograph of a cantilever milled within the polycrystalline zone of a single splat. It can be seen in the inset, electron backscatter diffraction (EBSD) mapping confirmed the polycrystallinity of the solidified structure. Applying the linear elastic bending theory for clamped beams, as proposed by [67], the largest stress at the interface is calculated:

$$\sigma = 6\frac{Fl}{wt^2} \tag{6}$$

here, F represents the loading force, l is the length of bending, w is the width, and t is the thickness of the beam.

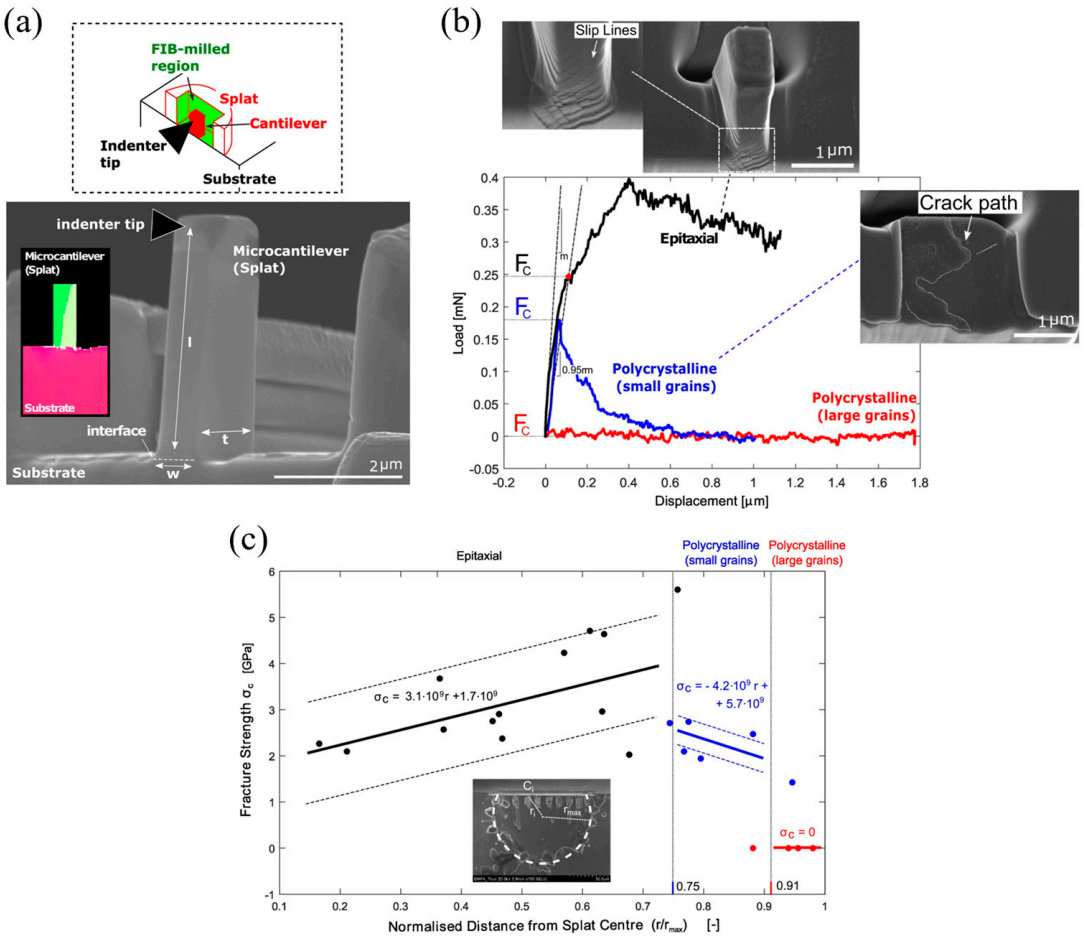

Figure 4. (**a**) SEM micrograph illustrating the dimensions and loadings used for examining FIB-milled cantilevers. The crystallographic orientation was determined via electron backscatter diffraction. (**b**) Load–displacement curves obtained from cantilevers milled in the three crystallization regions of a single splat, along with respective post-bending SEM micrographs obtained at the interface. (**c**) The calculated fracture strength as a function of the normalized distance from the splat center; uncertainty was determined as the standard error of regression in each region [59].

It was observed in Figure 4b that within the epitaxial area, the material first exhibited a linear elastic phase before transitioning into plastic deformation, which was evidenced by slip lines at the cantilever base. Crucially, no interface crack propagation occurred in any specimens tested from this area, a finding confirmed by the absence of load drops in their

respective curves. Considering the lack of a critical load (F_c) for the direct application of Equation (6), an ad hoc value was determined at 95% of the curve's slope in the linear elastic region. This method, therefore, provided an underestimation of the precise adhesion strength.

Conversely, a load drop, indicative of interfacial crack initiation, was measured within the polycrystalline zone outside the epitaxial area. In these cases, F_c was defined as the magnitude of the load drop. For cantilevers located in the polycrystalline zone at the periphery, no load was recorded, implicating minimal adhesion existed prior to the indentation. Figure 4c illustrates the calculated fracture strength as a function of the normalized splat radius for all tested cantilevers across different solidification zones. Linear fitting is presented, along with the norm of the residuals. Strength increased from the splat center toward the edge within the epitaxial zone, likely influenced by impact pressure and temperature effects. Conversely, a decrease in fracture strength was observed within the polycrystalline area characterized by small grain sizes. Lower splat–substrate interdiffusion and edge curling stress relaxation are responsible for the reduced adhesion observed. This reduction is relative to the epitaxial zone and is most pronounced toward the outer rim.

2.5. Scratch Test

The scratch test is a widely adopted method for assessing the shear strength of single splats. Sabiruddin and Bandyopadhyay performed some of the first scratch tests on single splats [60]. In their work, Al_2O_3 splats deposited on Ni–5wt.%Al and Ni–20wt.%Cr bond coats were subjected to scratching using a Rockwell C-type conical diamond indenter with a radius of 200 μm, at speeds of 0.1 or 0.2 mm/s. A fixed normal load, ranging from 1 to 6 N, was applied during scratching, and images of the scratched splats were used to evaluate scratch resistance. Figure 5a provides a schematic representation of this scratch testing procedure. Scratch resistance increased with splat thickness and decreased with the presence of a semi-molten phase, which acted as a defect. Furthermore, the extent of splat damage intensified with the increasing scratching speed and normal loading.

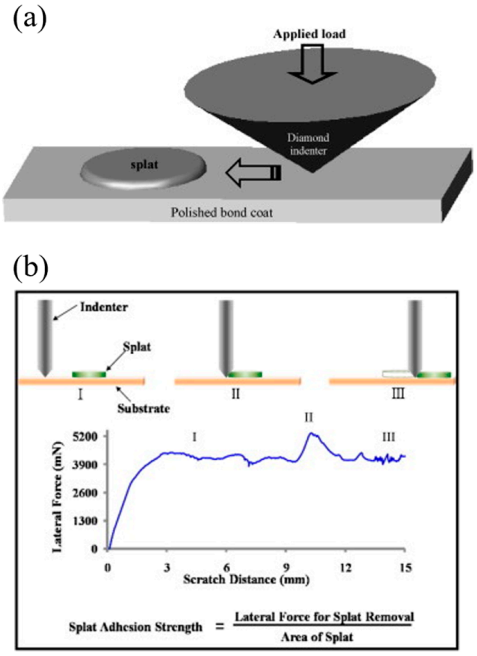

Figure 5. (**a**) Schematic representation of the scratch testing procedure on splats [60], (**b**) schematic of the scratch test on the single splat, where a typical lateral force vs. scratch distance curve during scratching on the single splat is shown. There are three stages. Stage I illustrates when indenter scratches on the bare steel substrate. Stage II is indicative of the indenter touching and dislodging the splat, which is reflected by the increase in the lateral force in the curve. Stage III shows a drop in the load after the indenter displaces the splat [61].

In the same year, a similar scratch method was employed to examine the bonding strength of carbon nanotube (CNT)-reinforced Al_2O_3 splats deposited on steel substrates, aimed at verifying the impact of CNT addition on the bonding strength [61]. As depicted in Figure 5b, the lateral force was recorded as a function of scratch distance. The adhesion force was then estimated by subtracting the lateral force on the bare steel substrate from the peak force observed during splat delamination. The splat's bonding strength was subsequently calculated as the ratio of the adhesion force to the splat area. CNTs significantly enhanced the adhesion strength of a single Al_2O_3 splat on steel substrates through two primary mechanisms of mechanical bonding: improved splat wettability due to the greater thermal conductivity and specific heat of CNTs, and enhanced mechanical interlocking caused by the anchoring effect of CNTs. Similar result was published by Jambagi [62].

The effects of adding hybrid CNTs and graphene nanoplatelets (GNPs) on the bond strength of Al_2O_3 splats was further investigated using nano-scratch tests [63]. The adhesion strength for pure Al_2O_3 was measured at 0.21 MPa, which increased to 1.08 MPa following the synergistic incorporation of CNTs and GNPs into the Al_2O_3 matrix. This improvement was primarily attributed to the nanofillers' high strength, enhanced melting of splats post-reinforcement, and superior interlocking between splats and substrates.

Chen et al. investigated the detailed debonding process during a micro-scratch test of Fe-based splats [64]. As illustrated by the splat debonding mechanism depicted in Figure 6a, upon contact with the splat, the forces acting on the indenter are defined by:

$$F_n = F_{nspl} + F_{nsub} \tag{7}$$

$$F_\tau = F_{\tau spl} + F_{\tau sub} \tag{8}$$

where F_n and F_τ are the normal and lateral forces on the indenter, F_{nsub} and $F_{\tau sub}$ are the normal and lateral forces exerted by the substrate on the indenter, and F_{nspl} and $F_{\tau spl}$ are the normal and lateral forces exerted by single splats on the indenter, respectively. The lateral force, penetration depth, and acoustic emission were recorded with respect to the scratch distance, as shown in Figure 6b–d for various substrate temperatures. Three distinct stages were observed during the dislodging process. The bonding strength is calculated as:

$$P = \frac{F_{\max} - F_{act}}{S} \tag{9}$$

P is the bonding strength, S is the area of debonding, and F_{max} is the maximum lateral force during the debonding process. F_{act} is the actual lateral resistance of the substrate on the indenter when the splat was debonded, which can be obtained by:

$$F_{act} = \begin{cases} \frac{kAH}{(R^2 - A^2)^{1/2}} & h > 0 \\ 0 & h \leq 0 \end{cases} \tag{10}$$

where A is the contact radius between the substrate and the indenter, R is the indenter tip radius, h is the penetration depth of the indenter into the substrate when the splat is dislodged, H is the indentation hardness of the substrate, and k is a constant varying between 0.2 and 1.0 [68]. Accurate estimation of the friction force should be critical to the accurate evaluation of the bonding strength because of the comparable magnitudes between the friction force and lateral force [69,70]. Generally, splats exhibit larger bonding strengths under higher substrate temperatures. Figure 6e–j display the periphery and center positions of the splat/substrate interface. It was found that good bond was achieved with surface temperatures of 400 °C; however, defects appeared under lower substrate

temperatures of 200 °C and 25 °C. The mechanism responsible for these poorly bonded areas is likely linked to the molten droplet's flattening process [71].

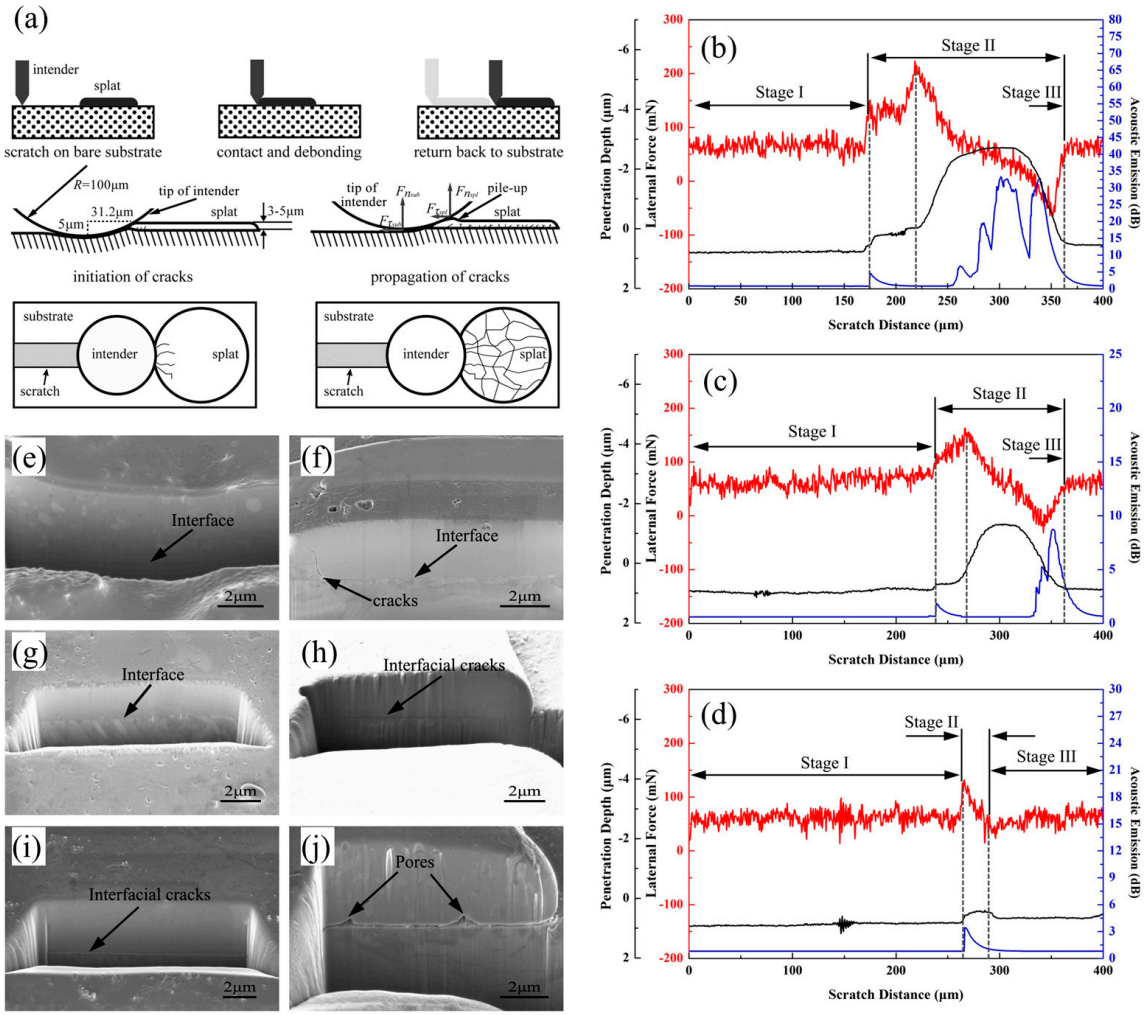

Figure 6. (**a**) Schematic of the splat debonding mechanism. Curves of the penetration depth, lateral force, and acoustic emission signals against scratch distance for splats deposited on substrates preheated to (**b**) 400 °C, (**c**) 200 °C, and (**d**) 25 °C. FIB/SEM morphologies of splat/substrate interfaces: (**e**,**f**) center and edge positions (400 °C), (**g**,**h**) center and edge positions (200 °C), and (**i**,**j**) center and edge positions (25 °C) [64].

2.6. Short Summary

The experimental techniques used to characterize the bonding strength of single splats, including tensile testing, scraping tests, indentation methods, microcantilever bending, and scratch testing have been comprehensively evaluated. Tensile and scraping tests offer relatively straightforward force measurements, but scraping is particularly useful for capturing interfacial failure under controlled loading. Nonetheless, these methods are more applicable to relatively soft materials and weak bonding. Stress concentrations at the loading point and the challenge of ensuring a pure tensile or shear loading condition dominate the reliability of these methods [72]. Indentation and microcantilever bending enable quantification of the fracture energy and local adhesion properties with high spatial resolution, though they necessitate complex sample preparation and advanced imaging tools such as FIB and SEM. Furthermore, milling-induced damage could be a major limitation for the microcantilever bending method. Scratch tests facilitate high-throughput evaluation and broad application; however, data processing remains challenging because of the variability in splat geometry and lateral force distribution.

Comparative analysis indicates that FIB-fabricated microcantilever bending and instrumented scraping tests provide accurate and localized assessments of adhesion, especially when supported by in situ or post-test imaging. Experimental results consistently demonstrate that higher substrate preheating temperatures and elevated impact velocities enhance bonding strength by promoting mechanical interlocking, localized plastic deformation, and metallurgical bonding at the splat/substrate interface. To improve experimental repeatability and enhance mechanistic understanding, future studies should develop characterization strategies that integrate quantitative force measurements with high-resolution imaging and real-time monitoring.

3. Testing Methods of the Residual Stress in Single Splats

Figure 7 illustrates the basic mechanisms of the development of residual stress for a single splat deposited on a substrate [34,73]. Initially, a tensile quenching stress forms within the splat as it rapidly cools to the substrate's preheating temperature. In addition to thermal contraction, quenching stress can be intricately linked to structural transformations in the rapidly cooling material where the volume change associated with the transformation creates significant transformation-induced stress that is superimposed on the thermal stress. This quenching stress can induce cracking perpendicular to the substrate surface, leading to a lamellar structure that is often found in thermal barrier coatings. Following rapid cooling, thermal stress arises as the splat and substrate cool down to room temperature, based on the thermal mismatch between the two materials.

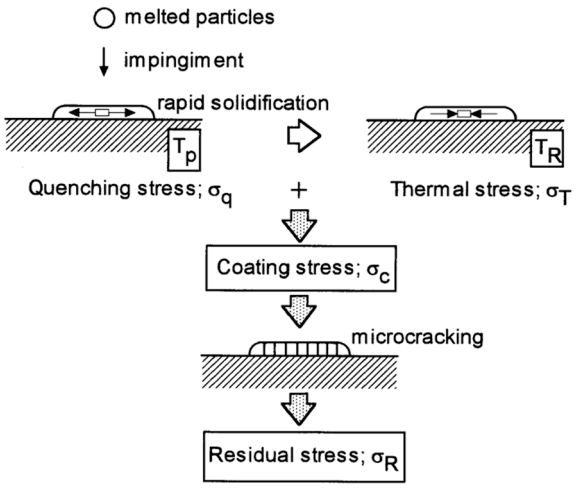

Figure 7. Schematic illustration of the impact and residual stress developed in a single thermally sprayed splat [73].

For ceramic splats on metal substrates, this thermal stress is compressive. This is because ceramics typically have a significantly lower coefficient of thermal expansion (CTE) than the metal substrate. During cooling, the metal substrate attempts to contract much more than the ceramic splat. Consequently, the final residual stress in the ceramics splat may be compressive, particularly with a high substrate preheating temperature or a significant thermal mismatch [74]. For metal splats like Molybdenum (Mo), which has a low CTE (~5×10^{-6} K^{-1}) deposited on common metal substrates like steel with a much higher CTE (~12×10^{-6} K^{-1}), a large thermal mismatch is evident. This mismatch is responsible for the induced compressive stress in the splat and, while it dominates the stress state, it is also important to consider thermal conductivity. For low thermal conductivity ceramic splats, the final stress state is highly susceptible to phase transformation stress and local temperature gradients. Conversely, for low-melting materials like wax or polymer splats, the combination of very low thermal conductivity and low deposition temperature

results in minimal heat transfer into the substrate, leading to a shallow thermal mismatch. Consequently, the low-magnitude residual stress in these systems is often dominated by a gentle tensile quenching stress rather than significant thermal mismatch stress.

A high impact velocity of the particles can also generate compressive peening stress due to plastic deformation, a dominant factor contributing to residual stress in cold spray deposits [14]. Although the residual stress in a single splat differs from that in a complete coating—being influenced by factors such as splat interaction—the stress at the splat level inevitably affects the final stress within the coating [75]. Table 2 summarizes the experimental techniques used for characterizing residual stress in single splats, which are reviewed in detail in the following subsections.

Table 2. Summary of the experimental techniques used to determine residual stress.

Splat Material	Substrate Material	Method	Residual Stress [MPa]	Reference
Mo	Steel, Al	XRD	~50 (tensile) ~200 (compressive)	[76]
Mo	Stainless steel	XRD	~1000 (compressive)	[77]
Mo	Stainless steel	XRD	~300 (compressive)	[78]
Mo	Stainless steel 304	XRD	75 (tensile)	[79]
YSZ	NiCrAlY bond coat + 316 stainless steel substrate	Raman spectroscopy	~2500 (tensile)	[80]
Ni–Al, Al_2O_3, Al_2O_3–TiO_2–ZrO_2–CeO_2	Ni–5wt.%Al bond coat + stainless steel substrate	FIB–DIC material removal	~110 (tensile) for Ni–Al splats ~500 (compressive) for other splats	[81]
CoNiCrAlY	Ni-based superalloy	HR-EBSD	~2000 (tensile)	[59]
Wax	Stainless steel 430	Reverse calculation from strain	–	[82]
Wax	Stainless steel 430	Reverse calculation from strain	~3 (tensile)	[83]
Wax	Stainless steel 430	Reverse calculation from strain	~3 (tensile)	[84]

YSZ, yttria-stabilized zirconia; XRD, X-ray diffraction; FIB, focused ion beam; HR-EBSD, high-resolution electron backscatter diffraction.

3.1. X-Ray Diffraction

X-ray diffraction (XRD) is the most widely used method for measuring the residual stress in thin coatings [85]. The $\sin^2\psi$ method is commonly used [86] because the spacing between the atomic lattice planes can reliably be determined based on Bragg's Law [87]. The first results for single splats may have been reported by Sampath and coworkers [76,77], where the residual stress of plasma-sprayed Mo splats on steel and aluminum (Al) substrates was measured by using a Bruker GADDS micro-diffractometer, employing Cr radiation and reflection from the (211) planes. They observed that for low substrate preheating temperatures, the tensile quenching stress dominates, and the final residual stress is therefore tensile. As the substrate temperature increases, the magnitude of the compressive thermal stress increases, causing the final residual stress to decrease. Under further increasing substrate temperature, the residual stress changes from tensile to compressive, and the magnitude of the final compressive residual stress increases with continuing increases in the substrate temperature. This is attributed to the greater CTE for the substrates, which generates compressive thermal stress in the coating, given that Mo has a much lower CTE than steel and Al.

These researchers also investigated the influence of spray power on residual stress, demonstrating that higher spray power led to a higher velocity and temperature of the impacted particles [78]. In this work, seven ψ-values ranging from -45° to 45° were used.

Figure 8a illustrates the measured residual stress under various spray powers, revealing that compressive stresses were present across all conditions. This is attributed to the significant thermal expansion mismatch between the steel substrate and the Mo splat, coupled with the substantial temperature drop (from approximately 200 °C to room temperature). The residual stress exhibits a decreasing trend with higher power spray conditions. At lower power conditions, the splats are larger and more contiguous, with minimal evidence of substrate melting. As a result, the stress is being retained within the splat itself. As shown in Figure 8b–d, at higher power conditions, the splats fragment to a greater extent, and a larger amount of substrate melting occurs. These phenomena can induce stress relaxation mechanisms in the splats, thereby resulting in a lower net residual stress. More recently, to verify their numerical model, Jia et al. used an XtaLAB Synergy-I micro-diffractometer (Rigaku Co., Tokyo, Japan) employing Cr radiation and reflection from the (211) crystal planes to measure the residual stress in air plasma-sprayed Mo splats bonded with stainless steel 304 [79].

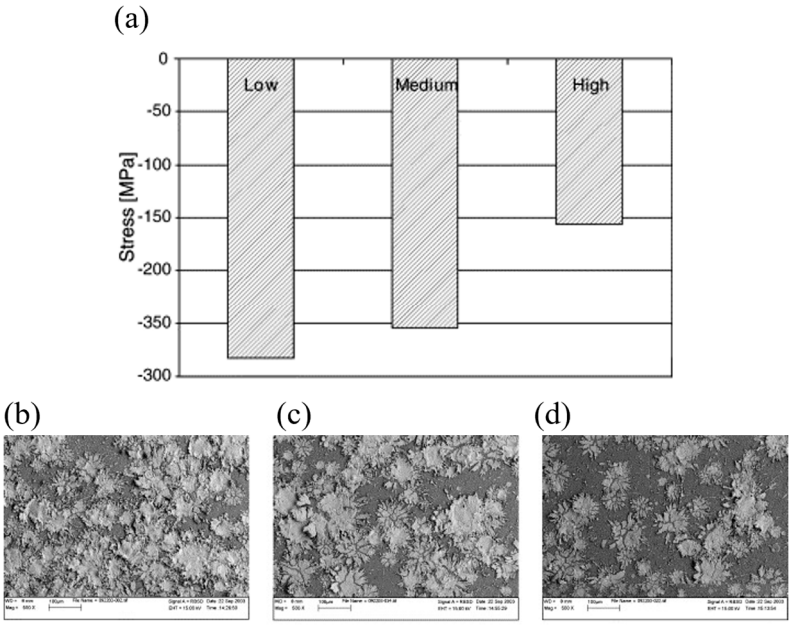

Figure 8. (**a**) Residual stress measured in Mo splats by XRD, thermal sprayed on stainless substrates under various spray powers. Micrographs of splats formed under (**b**) low, (**c**) medium, and (**d**) high spray power conditions [78].

3.2. Raman Spectroscopy

Considering that Raman spectroscopy can effectively determine strain for materials like ZrO_2, which possesses a Raman-active tetragonal phase, and given the linear relationship between the stress in ZrO_2 coatings and the Raman shift, this technique was employed to investigate the residual stress of plasma-sprayed and laser-remelted ZrO_2 splats [80]. The as-received ZrO_2 powder was ground and assumed to be stress-free. Then, splats were thermally sprayed onto a 316 stainless steel substrate with an intermediate NiCrAlY bond coat. During the test, a He-Ne laser with a wavelength of 633 nm was used to irradiate the splats. Raman spectroscopy of the as-received powder was performed first, and a tetragonal peak observed at 638.35 cm^{-1} was chosen as a reference. A peak shift above this wavenumber indicates compressive residual stress, and vice versa. A shift of 1 cm^{-1} corresponded to a residual stress of 220 MPa according to a Raman shift—applied stress plot [88]. Figure 9a,b illustrate the variation in residual stress within a single splat deposited at different in-flight particle velocities and temperatures, where the stresses were always in tensile. Contrary to other reported findings [78], no relationship was observed between the

residual stress and either the particle velocity or temperature. Figure 9c presents a laser-remelted ZrO_2 splat with a dendritic structure present on its top surface. Figure 9d displays the stress retained in a set of laser-remelted splats. The average stress in remelted splats is significantly lower than that of an as-sprayed splat. Notably, a laser-remelted splat forms a large molten pool that cools more slowly than an as-sprayed splat; the associated cooling rates during plasma spraying and laser remelting are approximately 10^6 and 10^2 K/s, respectively [89]. Moreover, the residual stress significantly decreased with a reduction in the substrate temperature, suggesting the dominant role of thermal stress in the residual stress of a single splat [77].

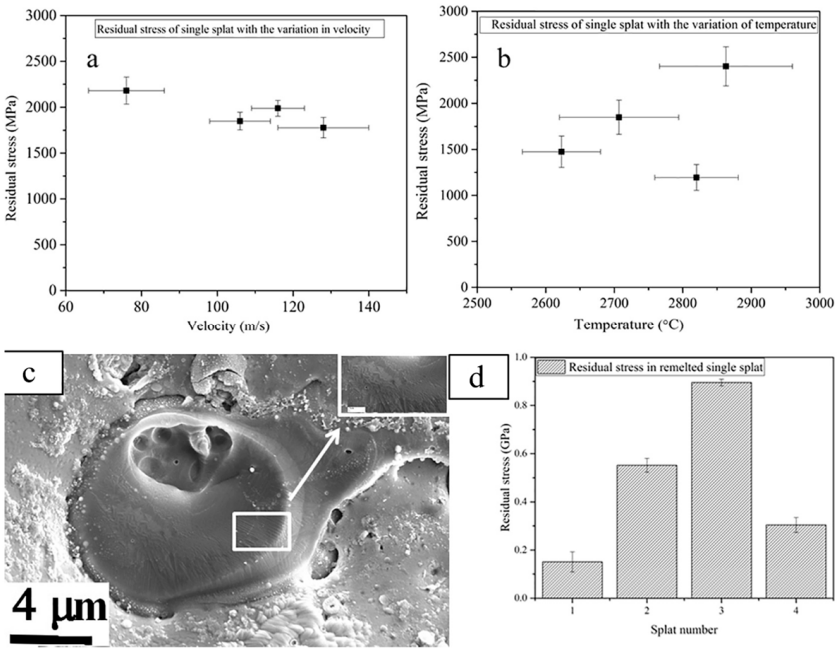

Figure 9. The measured residual stress of ZrO_2 splats deposited on 316 stainless steel substrates under various (**a**) velocities and (**b**) temperatures. (**c**) Photographs of a remelted ZrO_2 splat. (**d**) Measured residual stress generated in laser-remelted splats [80].

3.3. Focused Ion Beam–Digital Image Correlation

Sebastiani et al. combined FIB microscale ring-core milling with digital image correlation (DIC) for relaxation strain mapping, providing sub-micrometer spatial resolution for residual stress evaluation in both splat microstructures and amorphous materials [81,90–92]. For splat measurements, a 100 nm thick platinum layer was initially electron-beam deposited onto a circular area (3 μm in diameter). Subsequently, a grid of small dots (each approximately 60 nm in diameter and depth) was exclusively milled in the platinum layer by FIB (Figure 10a). The operation created a reference surface for relaxation strain analysis that was intended to be unaffected by milling artifacts [90–92]. A trench with an inner diameter of 3 μm was milled stepwise using FIB around the platinum-coated region. High-resolution SEM graphs of the patterned area were acquired before and after each milling step (Figure 10b,c). The progressive increase in trench depth led to the relaxation of residual stresses within the circular core, generating measurable surface deformation. DIC analysis utilized the series of high-resolution micrographs acquired during the milling steps to map the relaxation strain profiles along two orthogonal axes for each fixed depth increment. The final step involved determining the average strain at a given depth by performing a polynomial fit on the complete set of strain data. Meanwhile, ion beam damage is expected to be negligible on the elastic recovery of the micron-sized splats, as the damage layer is typically smaller than 20 nm from the cut edge. The effect of Pt-layer compliance on the relaxation strain profile is significantly reduced by depositing the layer using the electron beam rather than the ion gun as a source.

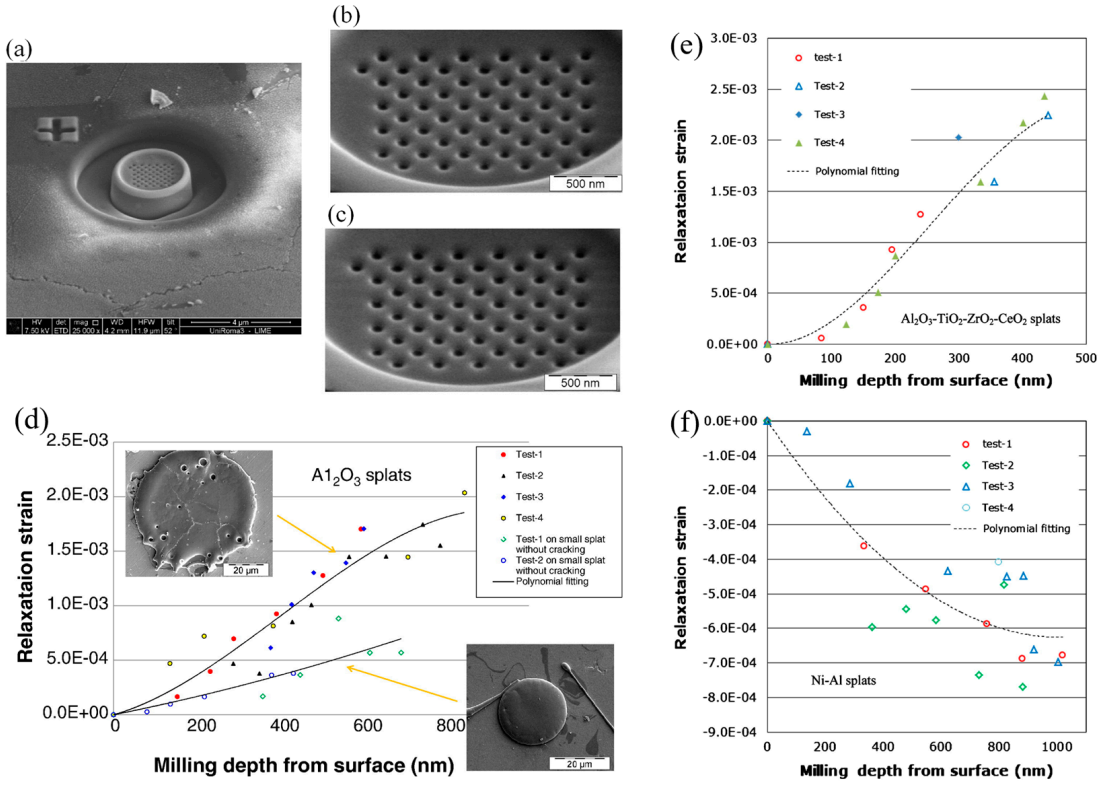

Figure 10. (**a**) Example of a micron-scale ring-core FIB–DIC test. (**b**) Example of a high-magnification micrograph acquired before and (**c**) after milling. (**d**) Relaxation strain vs. milling depth for the Al_2O_3 splats for both large (microcracks) and small (no cracks) splats, with SEM images of splats. (**e**) Relaxation strain vs. milling depth for the Al_2O_3–TiO_2–ZrO_2–CeO_2 and (**f**) Ni-5wt.%Al splats [81].

Ni–5wt.%Al, Al_2O_3, and (Al_2O_3–13wt.%TiO_2)–8wt.%ZrO_2–8wt.%CeO_2 single splats were plasma sprayed onto a Ni–5wt.%Al bond coat that was first sprayed onto a stainless steel substrate. The relaxation x-strain versus milling depth profiles, acquired through incremental FIB ring-core milling and DIC, are presented in Figure 10d–f, alongside the polynomial fitting of the experimental data. No significant difference was found between the x- and y-strains, suggesting an equal–biaxial stress state. In Al_2O_3 splats, quenching stresses were relieved through microcracking once those stresses exceeded the material's tensile strength. Conversely, the Al_2O_3–TiO_2–ZrO_2–CeO_2 lamellae derived from agglomerated nanostructured powders, developed a glassy structure owing to the suppression of crystallization phenomena. Consequently, these quenching stresses dissipated without crack formation, a phenomenon attributed to viscous flow above the glass transition temperature. These stress-free, non-cracked glassy splats may be a critical determinant for the overall strength and toughness of Al_2O_3–TiO_2–ZrO_2–CeO_2 coatings. In contrast, the stress condition of Ni–Al splats was primarily governed by quenching stress, which was only partially accommodated by edge curling and/or yielding.

3.4. High-Resolution Electron Backscatter Diffraction via Cross-Correlation-Based Pattern Shift Analysis

Fanicchia et al. measured the residual stress in thermally sprayed CoNiCrAlY single splats employing a high-resolution EBSD (HR-EBSD) method [59]. Residual stresses and the geometrically necessary dislocation (GND) density were determined by HR-EBSD using cross-correlation-based pattern shift analysis [93]. The presence of GNDs in crystalline materials ensures local continuity following plastic flow. Because their density (ρ_{gnd}) is proportional to the gradient in local lattice rotation, this metric can quantify the stored plastic strain [94]. In their work, the GND density was determined using Nye's

approach [95]. this calculation utilizes the lattice curvature tensor that is itself derived from cross-correlation pattern shift analysis. The density obtained via this method represents a lower bound of the total dislocation density [96]. Figure 11 displays (a) the calculated GND density and (b) the normal component of the linear elastic residual stress state in the specimen's *Y*-direction. The measured tensile in-plane linear elastic residual stress registered maximum levels of 1–2 GPa across the splat and the substrate. In the substrate, this pressure decreased moving away from the splat's central axis. The measured stress is lower than the theoretical quenching stress (6.8 GPa), confirming the significant influence of stress relaxation mechanisms.

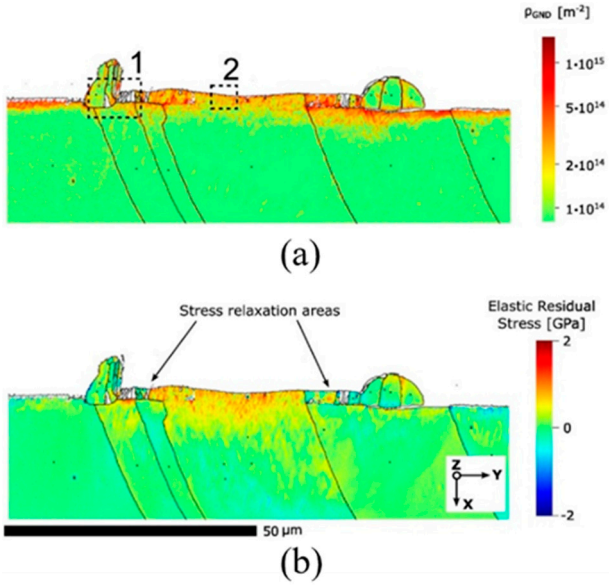

Figure 11. (**a**) Distribution of the GND density within and below the single splat cross-section, illustrating the tendency for slip system activation. (**b**) In-plane linear elastic residual stress, showing a radially decreasing trend from the splat center and a low magnitude in areas corresponding to the onset of polycrystalline growth [59].

3.5. Strain Evolution Measured Using Strain Gauges

The evolution of quenching strain during the impact and solidification of a single molten droplet was thoroughly investigated by Sakaguchi and coworkers [82–84]. They developed a free-fall drop impact testing setup (Figure 12a), which enabled the precise control of the droplet temperature, substrate temperature, and impact velocity. A bi-axial strain gauge and several thermocouples were attached to the back surface of the stainless-steel substrate to monitor its strain and temperature during the impact and deposition of a paraffin wax droplet. The measured total strain (ε_{total}) consists of three components:

$$\varepsilon_{total} = \varepsilon_q + \varepsilon_a + \varepsilon_c \quad (11)$$

where ε_q represents the quenching strain resulting from the solidification and rapid cooling of impacted splats. ε_a and ε_c are thermal strains induced by the thermal mismatch between the substrate and the strain gauge and by the temperature distribution in the substrate due to transient heat transfer from the droplet, respectively. ε_a and ε_c were determined from pre-tests and subsequently subtracted from the measured total strain (ε_{total}) to obtain ε_q. Typical quenching strain and temperature values are plotted as a function of the time after impact in Figure 12b, illustrating a scenario where three splats were deposited in a piled-up manner. Here, the two quenching strains, namely ε_q(Ch. 1) and ε_q(Ch. 2), measured using the bi-axial strain gauge, exhibited comparable magnitudes. This confirms that in-plane equi-biaxial strains, ε_{rr} and $\varepsilon_{\theta\theta}$, are generated in both the substrate and the splat. The tensile

quenching strain increased as the number of droplets increased but decreased at the third drop because of interfacial delamination. As plotted in Figure 12c, ε_q at the steady state of the first drop was found to increase with a reduction in substrate temperature, owing to a greater temperature drop from the stress-free temperature. A higher quenching strain was measured under a lower impact velocity of 0.99 m/s, compared with 1.4 m/s. This may be caused by the formation of a thicker splat at lower impact velocities. However, the quenching strain was significantly released when cracking or interfacial debonding occurred, indicating that the quenching stress had exceeded the splat's strength.

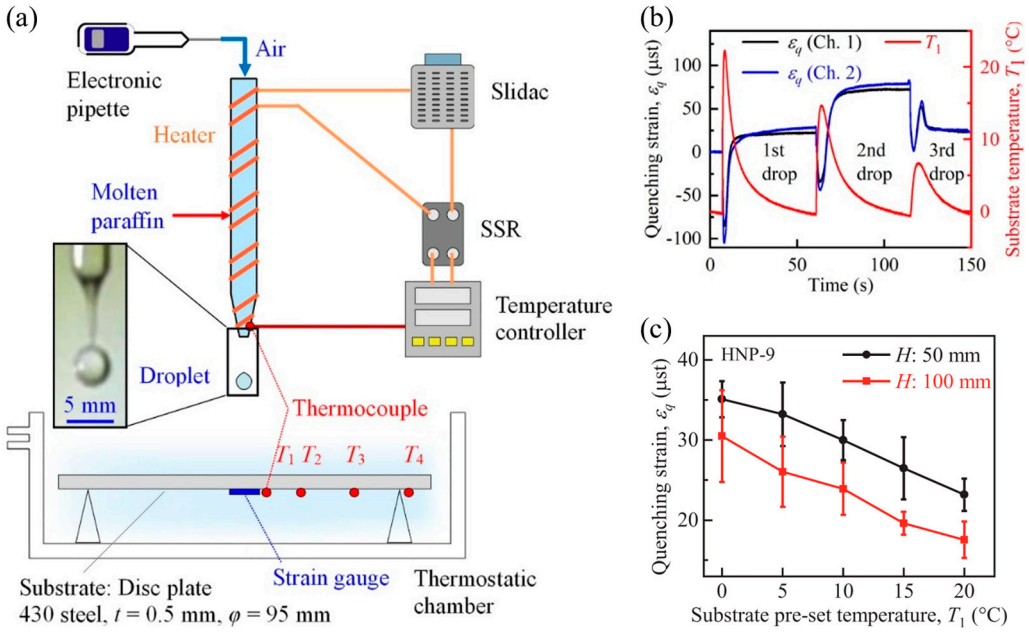

Figure 12. (**a**) Experimental setup. (**b**) Typical measurements of the evolutions of quenching strains (ε_q) and substrate temperature (T_1). (**c**) Measured ε_q during the steady state of the first drop as a function of T_1 at impact velocities of 0.99 m/s (H = 50 mm) and 1.4 m/s (H = 100 mm) [83].

3.6. Short Summary

The methodologies developed for characterizing residual stress in individual splats have been reviewed herein, emphasizing techniques such as XRD, Raman spectroscopy, FIB–DIC, HR-EBSD, and embedded strain gauge measurements. XRD and Raman spectroscopy provide average stress information, with Raman being particularly effective for ceramic splats with suitable Raman activity. Conversely, FIB–DIC and HR-EBSD offer superior spatial resolution and can resolve stress and strain fields at the sub-splat scale. Strain gauge methods enable real-time dynamic stress monitoring during droplet impact but are limited to splats with low temperatures and moderate velocities. The reviewed literature highlights a consistent trend: increasing the substrate temperature significantly reduces the quenching-induced tensile residual stress, which is due to slower thermal gradients and enhanced compliance at the splat/substrate interface. A promising direction for future research lies in combining in situ stress monitoring (e.g., strain gauges) with high-resolution post-deposition analysis (e.g., FIB–DIC), thereby achieving more complete temporal and spatial mappings of stress evolution and relaxation phenomena. Furthermore, future work must leverage advancements in non-contact diagnostics to directly measure splat mechanical characteristics. This includes employing advanced methods such as high-resolution, in situ high-speed imaging [97,98] for transient fluid dynamics, synchrotron X-ray diffraction [99] for instantaneous residual stress and phase changes, and Infrared thermography [100,101] for real-time interfacial heat flux, moving beyond conventional ex situ measurements that dominate the current single-splat literature.

4. Analytical Models and Numerical Simulations of the Residual Stress in Single Splats

4.1. Analytical Models

The analytical models and numerical simulations for predicting residual stress are summarized in Table 3. The lateral stress generated in a single splat was first analyzed by Kuroda et al., as illustrated in Figure 13a [34]. A simple equation was proposed to represent the maximum quenching stress:

$$\sigma_0 = \alpha_d \Delta T E_0 \tag{12}$$

where α_d is the CTE of the splat, ΔT is the difference between the melting point of the splat and the substrate temperature, and E_0 is the splat's elastic modulus. When interfacial adhesion between the splat and the underlying solid is perfect, and the splat undergoes a sufficiently large temperature change during cooling, a lateral tensile stress can readily emerge. This stress often greatly exceeds the material's yield strength under uniaxial loading. This phenomenon arises because plastic flow is strongly constrained in a thin film adhered to a rigid substrate. However, several stress relief mechanisms can lower the stress within the splat below its theoretical maximum value, σ_0 (Figure 13b). For instance, if the material exhibits brittle behavior, microcracking provides a significant means of reducing the internal strain. Assuming ideal bonding between the deposit and the substrate and purely elastic behavior during the cooling phase, the final residual stress, $\sigma_r(T_0)$, can be expressed simply as the summation of the quenching stress and the stress originating from differential thermal contraction:

$$\sigma_v(T_0) = \left(\sigma_q(T_s)/E_d(T_s) + (\alpha_d - \alpha_s)(T_s - T_0)\right)E_d(T_0) \tag{13}$$

here, $\sigma_q(T_s)$ represents the average lateral stress that develops in the splats, $E_d(T)$ is the coating's elastic modulus at temperature T, and α_d and α_s denote the thermal expansivity values for the deposit and the substrate, respectively. However, a discrepancy is frequently noted between theoretically forecast and measured stress values, primarily due to various stress relaxation activities. Therefore, a correction coefficient is required for accurate stress prediction [102]. As presented in Section 4.2, additional correlation coefficients were proposed by Jia et al. [79] to predict the deposition stress more accurately, based on comparisons between theoretical and experimental/numerical results.

Table 3. Summary of the analytical methods used to determine residual stress.

Splat Material	Substrate Material	Deformation	Method	Code	Reference
-	-	Elastic	Elastic model	-	[34]
Mo	Stainless steel 304	Elastic	Elastic model with correction coefficients	-	[79]
YSZ	Steel alloy	Elastic–plastic	SPH-FEM	ABAQUS/Standard + ABAQUS/Explicit	[103]
Mo	Stainless steel 304	Elastic	VOF + FEM	FLOW-3D + ABAQUS	[79]
Carbon steel	Carbon steel	Elastic, creep	FEM	ABAQUS	[104]
Al alloy, Bi	Steel	Elastic	FEM	ANSYS 10.0	[105]
YSZ	Stainless Steel	Elastic–plastic	FEM	ABAQUS/Explicit	[106]
Wax	Stainless steel 430	Elastic	FEM	ABAQUS/Standard	[83]
Wax	Stainless steel 430	Elastic, creep	FEM	ABAQUS/Standard	[84]

YSZ, yttria-stabilized zirconia; SPH, smooth particle hydrodynamics; VOF, volume of fluid; FEM, finite element method.

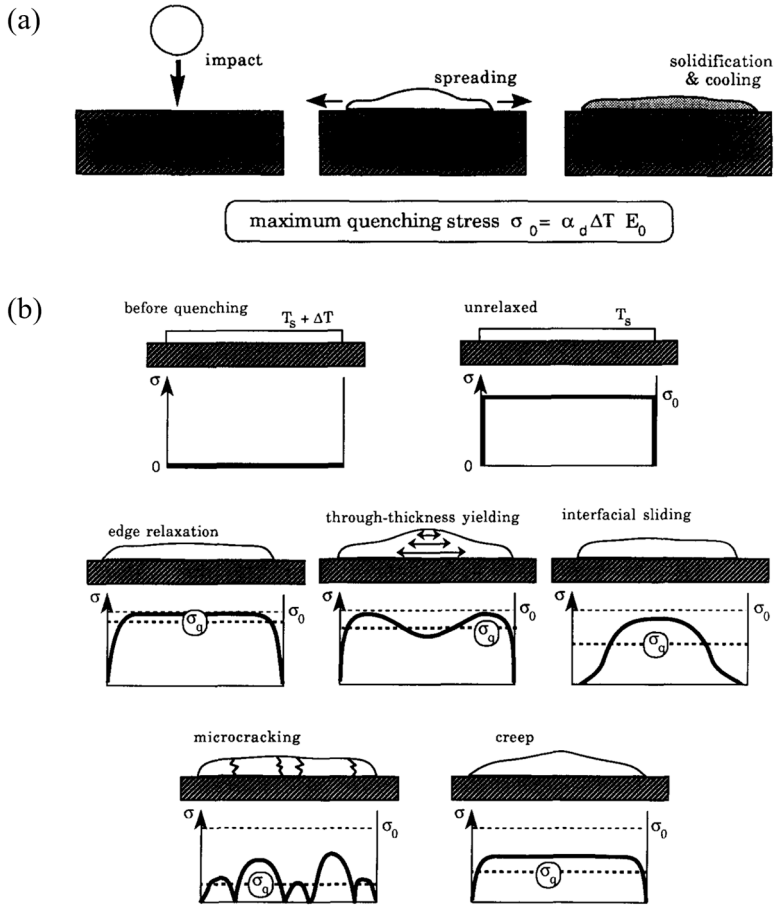

Figure 13. (**a**) Schematic depiction of the impact, spreading, and cooling of a single splat. (**b**) Schematic illustration of the stress distributions within a single splat before and after various forms of stress relaxation [34].

4.2. Numerical Simulations

Numerical prediction of the stress generated in individual splats dates back to 1996, when Chin et al. proposed 2D thermal and mechanical models using the finite element method (FEM) [104]. These models investigated the transient and steady-state temperature and stress within a single, initially molten metal droplet deposited onto a comparatively large substrate, focusing on its centerline. Both the droplet and substrate materials are carbon steels. The dimensions of the 2D model and the thermal and mechanical boundary conditions used to simulate a typical micro-casting scenario are shown in Figure 14a,b. A secondary creep constitutive model for a medium carbon steel in the austenitic phase is utilized to capture time-dependent creep:

$$\dot{\varepsilon} = A(\sinh(B\sigma))^n \exp\left(-\frac{C}{T}\right) \tag{14}$$

where $\dot{\varepsilon}$ is the creep strain rate, σ is the Mises stress, and T is the absolute temperature. A, B, C, and n are fitted constants. Figure 14c,d presents the centerline radial stress distributions at discrete times and different substrate-preheat temperatures, indicating that high steady-state tensile stresses are generated in the deposited droplet and the top portion of the substrate. These tensile stresses extend approximately 2.5 droplet thicknesses into the substrate. Additionally, moderate levels of preheat can significantly reduce residual stresses. This reduction in stress magnitude is accompanied by an increase in the depth to which residual tensile stresses are present in the substrate. Xue et al. used ANSYS, a commercial finite element (FE) code, to simulate heat transfer during the cooling of the splat and the

substrate, as well as examine splat deformation caused by thermal stresses [105]. The splat–substrate system was assumed to be thermo-elastic, and the calculation results for the thermal stress with different assigned curling-up angles are provided in Figure 14e–g.

Recently, several numerical studies have investigated the stresses in individual impacting particles [79,83,84,103,106,107]. Abubakar et al. developed a hybrid model combining a point cloud (PC) and FEs to simulate the spray process and associated residual stresses in yttria-stabilized ZrO_2 (YSZ) splats deposited on SS310 [103,107]. Plastic deformation was simulated using the von Mises criterion. Droplet deposition modeling and associated deformation were modeled using a PC and smooth particle hydrodynamics (SPH), a meshless approach developed for simulating violent fluid flows. The conversion of the PC to an FE mesh of the splat was achieved using various algorithms [108–111] designed for PC processing, as illustrated in Figure 15a–d. Using the numerically generated FE mesh, FE analysis was conducted to effectively predict the temperature evolution and residual stresses during the process. The distribution of residual stress along the axial and radial directions is presented in Figure 15e,f, and the colormap for stress distribution along the *x*- and *y*-directions is given in Figure 15g,h. Figure 15e shows that the compressive residual stresses developed in the near-interface region of the coating are balanced by corresponding tensile stresses on the substrate side. Figure 15f indicates that an equi-biaxial residual stress field develops in the coating layer. Furthermore, higher compressive stresses are observed at the edges of the splat than at the center owing to the thinness of the edges.

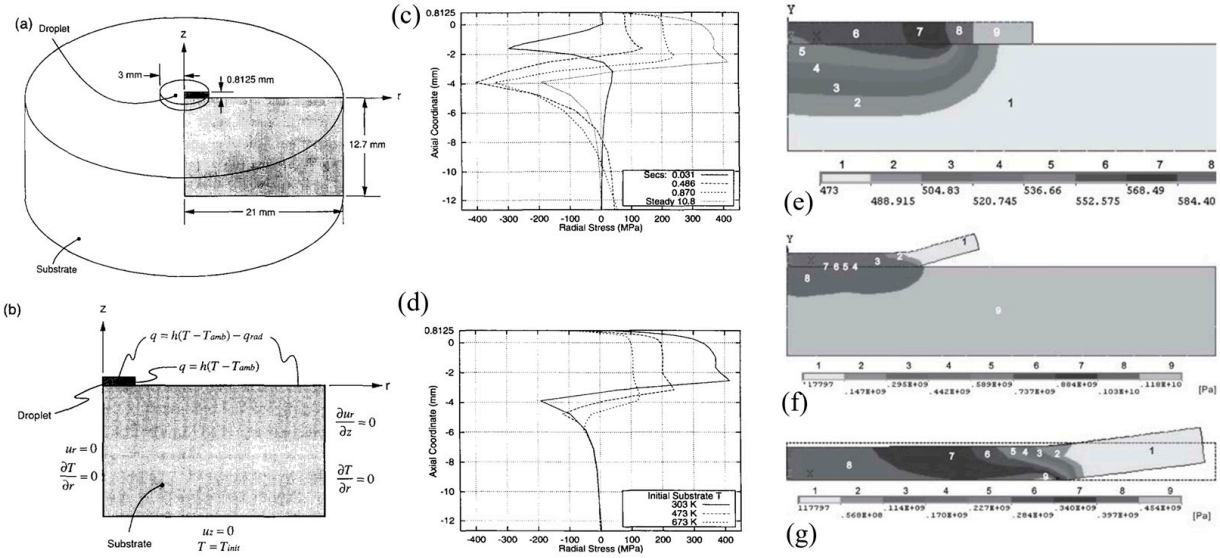

Figure 14. (**a**) Dimensions of 2D model. (**b**) Thermal and mechanical boundary conditions of the 2D model. (**c**) Centerline radial stress distributions at discrete times. (**d**) Effect of substrate preheat on steady-state radial stress distributions [104]. (**e**,**f**) Typical simulation results of the temperature distribution and structural deformation of the aluminum alloy splat and tool steel substrate at time 0.1 s: (**e**) temperature distribution, (**f**) stress distribution. (**g**) Magnified stress distribution and deformation of the splat (temperatures are in K, stresses are in Pa) [105].

Fardan et al. employed ABAQUS/Explicit and the Eulerian method to model the residual stress for molten YSZ splats (30 µm in diameter) impacting stainless steel substrates at velocities of 100, 150, 190, and 240 m/s [106]. Considering the high impact velocity and temperature, the elastic–plastic response of the stainless steel and YSZ splat was calculated using the Johnson–Cook model:

$$\sigma = (A + B\varepsilon^n)\left(1 + C\ln\dot{\varepsilon}^*\right)(1 - T^{*m}) \quad (15)$$

here ε is the plastic strain, $\dot{\varepsilon}^* = \dot{\varepsilon}/\dot{\varepsilon}_0$ is the dimensionless plastic strain rate, and T^* is the homologous temperature. A, B, C, n, and m are the static yield strength, strain-hardening exponent, strain-rate-sensitive coefficient, strain-hardening modulus, and thermal-softening exponent, respectively. The low thermal conductivity of the ceramic powder induces a temperature gradient. The temperature-dependent viscosity is expressed by:

$$\mu = 0.1 \exp\left(-2.95 + \frac{5993}{T}\right) \tag{16}$$

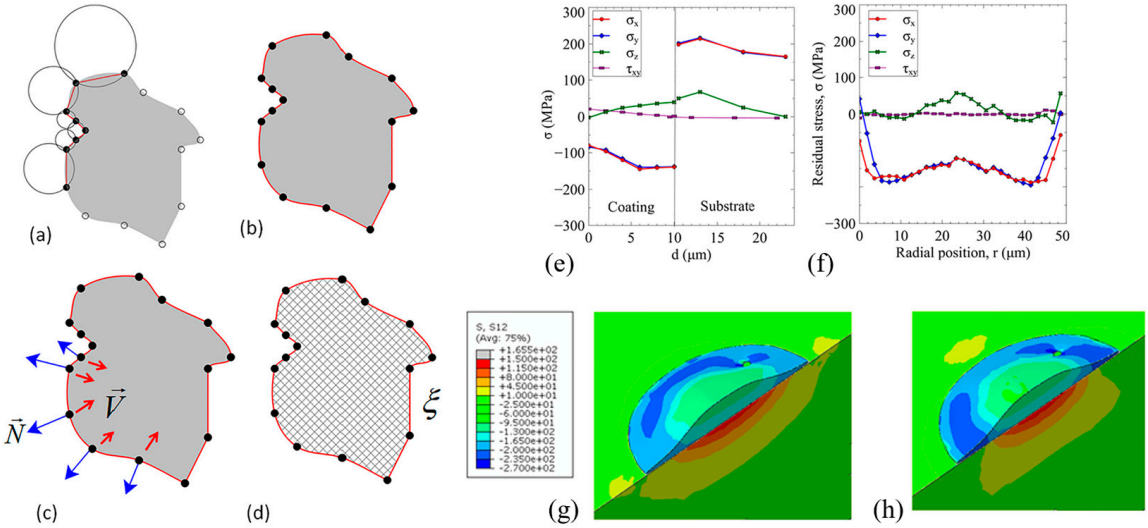

Figure 15. (**a**,**b**) Surface topology identification using alpha shape. (**c**,**d**) Generation of the STL mesh using normal vectors at point sets and Poisson surface reconstruction. (**e**) Residual stress profile along the axial direction and (**f**) the radial direction. Residual stress developed in the (**g**) *x*-direction and (**h**) *y*-direction for a single splat [103].

Figure 16 presents the evolution of in-plane residual stresses acting in the XZ plane for an initial substrate temperature of 423 K with a YSZ particle impacting at 240 m/s and an initial particle temperature ranging from 3250 to 3067 K. Figure 16a shows the residual stresses in the YSZ particle, and Figure 16b shows the residual stresses in the stainless steel substrate. The effect of thermal contact resistance was verified, and it was found to influence the through-thickness residual stresses in both the coating and the substrate. The nature of the stresses remains the same, but the magnitude obtained for lower thermal conductance is slightly higher.

Kang et al. developed an elastic and a coupled thermomechanical FE model to estimate the distribution and evolution of the stress and strain during the cooling of a paraffin droplet free-fall impacting a stainless-steel substrate [83,84]. A 2D axial–symmetric model, illustrated in Figure 17a, was used to calculate the residual stress distribution of the deposited splat based on experimentally measured quenching strain at the substrate's back surface, as described in Section 3.5. A static elastic simulation was performed, where thermal stress was generated by the splat's temperature drop from a specific temperature, T_{sf}, to the substrate preheating temperature. The factors influencing residual stress, such as creep and interfacial defects, were neglected, and the value of T_{sf} was determined so that the calculated quenching strain equaled the measured value; therefore, the calculated stress distributions were also identical to the actual stresses. Figure 17b,c summarize the residual radial stress at the substrate center as a function of substrate temperature and impact velocity for two types of splat materials. The residual radial stress was found to increase with decreasing substrate preheating temperatures, attributed to a greater temperature drop from the stress-free temperature. Additionally, higher radial stress was

calculated under a greater impact velocity (free-falling height). The residual stress was significantly released upon the appearance of cracking when the residual radial stress exceeded the material strength. Figure 17d,e show distributions of the peeling stress, σ_{zz}, and shear stress, τ_{rz}, along the splat/substrate interface as a function of the distance from the center under various substrate temperatures. The maximum tensile peeling stress and maximum shear stress are located at the periphery of the splat and increase with decreasing substrate temperatures. These results align well with experimental observations of interfacial debonding, which are more likely to occur at lower substrate temperatures and initiate at the periphery.

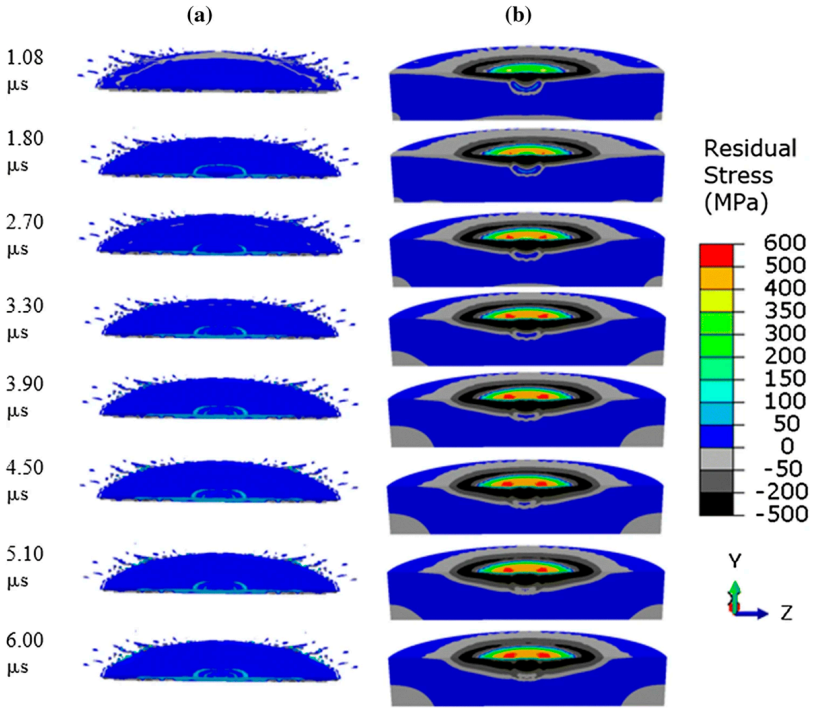

Figure 16. Residual stresses acting in the XZ plane for an initial substrate temperature of 423 K with a YSZ particle impacting at 240 m/s, and the initial temperature of the particle ranges from 3250 to 3067 K. (**a**) Residual stresses in the YSZ particle (sectional isometric view). (**b**) Residual stresses in the stainless-steel substrate (front view) [106].

To directly calculate and verify the evolution of strain at the substrate's back surface during the cooling of the paraffin splat, a coupled thermomechanical simulation was performed, incorporating creep deformation using a time-hardening model:

$$\dot{\varepsilon} = A\sigma^n t^m \tag{17}$$

where ε is the creep strain, σ is the stress, and t is the creep time. A, m, and n are temperature-dependent constants, determined by a four-point bending test with a temperature interval of 5 or 10 °C from the splat's stress-free temperature to the substrate preheating temperature. The temperature-dependent elastic modulus of the splat was measured by a three-point bending test, and the stress-free temperature was defined as the value when the elastic modulus is almost zero [84]. Figure 17f,g present a comparison of the quenching strain evolution determined by measurements and simulation, where the red curve indicates that creep was neglected and the blue curve refers to the inclusion of creep deformation in the simulation model. It can, therefore, be concluded that approximately one-third of the quenching strain was released by creep deformation, suggesting significant stress relaxation due to high-temperature viscous deformation. However, the calculated value was still

almost twice that of the measurements, implying that other factors, such as interfacial sliding or defects, may contribute to stress release.

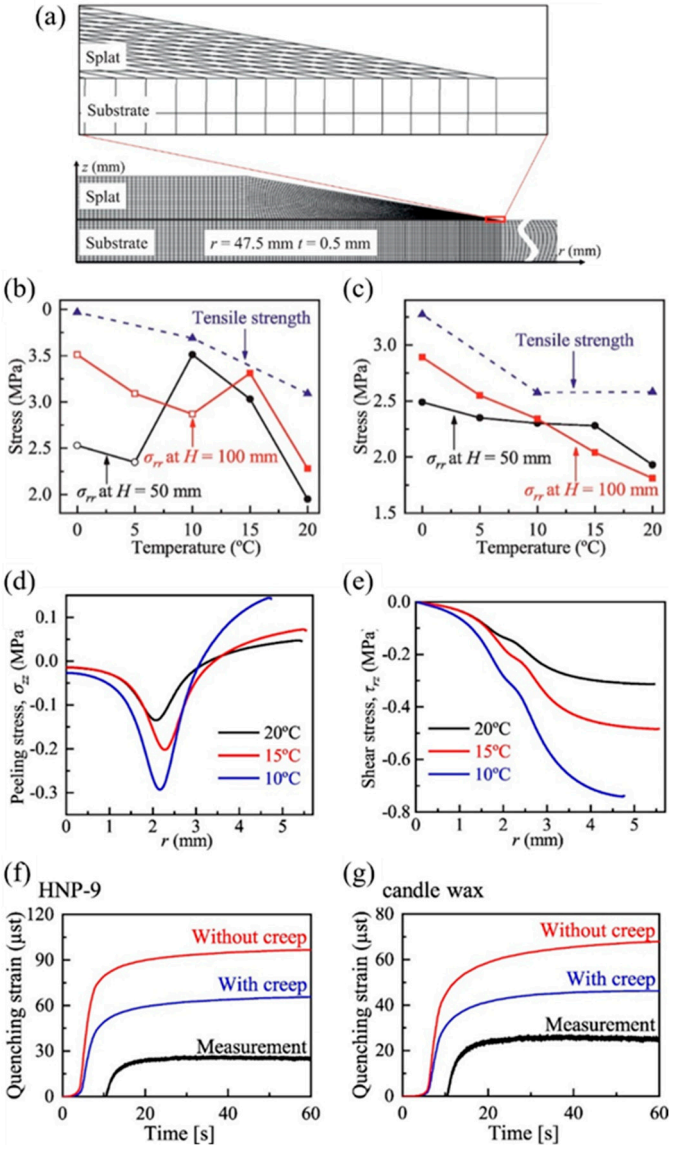

Figure 17. (**a**) 2D axial–symmetric model. (**b**,**c**) Splat stress (σ_{rr}) and tensile strength for (**b**) candle wax and (**c**) HNP-9 with a changing pre-set substrate temperature at drop heights of 50 and 100 mm. Open symbols in (**b**) indicate that cracking occurred. (**d**,**e**) FEM results for (**d**) peeling stress (σ_{zz}) and (**e**) shear stress (τ_{rz}) distributions along the interface when substrate pre-set temperatures were 10, 15, and 20 °C [83]. (**f**,**g**) Comparison of experimental and numerical results for quenching strain variation under a pre-set substrate temperature of 20 °C and a drop height of 50 mm for (**f**) HNP-9 and (**g**) candle wax [84].

Recently, Jia et al. used VOF and FEM to analyze the evolution of residual stress during the deposition of single splats on a groove-patterned surface prepared by laser surface texturing, in the context of Mo droplet deposition [79]. The measured groove profile data were used to construct a groove for the numerical model of the substrate, as shown in Figure 18a. The standard Flow-3D mesh was employed to generate the new FE mesh for the groove wall and solidified regions. When tetrahedron elements were used, the standard grid was split into five tetrahedra, as shown in Figure 18c,d. To maintain the interface's position, a network of springs was implemented at different nodal locations. The springs were intentionally weak to avoid altering the stress field, but possessed adequate

stiffness to ensure the desired stability, as presented in Figure 18e. The calculation results for variations in mean isotropic deposition stress within the splat are presented in Figure 18f. The von Mises stress located at the splat's bottom center interface is displayed in Figure 18g. The distribution of the maximum principal deposition stress is shown in Figure 18h. All findings indicate that deposition stress is created within the splat's solidification layer as the droplet solidifies, leading to a tensile stress state. The splat's mean isotropic stress measures 176 MPa and is primarily localized at the interface. The von Mises equivalent stress also peaks at the interface, reaching a maximum value of 141 MPa at the top surface. Conversely, the groove walls experience compressive stress, with its maximum value situated at the center of the spreading area. Deposition-induced stress causes cracking, yielding, and slipping within the splat, resulting in a 24.6% reduction in magnitude due to stress relaxation. Correction coefficients for the theoretical equation predicting deposition stress are λ = 0.119 (from simulation) and 0.096 (from experimentation), respectively. Furthermore, the deposition stress diminishes with an increase in deposition temperature:

$$\sigma_{dc} = \frac{E_c}{1-\nu_c}\alpha_c\lambda(T_0 - T_d) \tag{18}$$

where E_c and υ_c are the coating's elastic modulus and Poisson's ratio, respectively. α_c is the coating's CTE. T_d and T_0 represent the deposition and initial droplet temperatures, respectively.

While offering robust solutions for complex geometries and material properties, FEM faces significant limitations in single-splat modeling, contributing to the difficulty in developing unified approaches. Accurately modeling phenomena across vastly different scales demands computationally prohibitive fine meshing and extremely short time steps. Furthermore, the need for accurate high strain-rate, non-linear constitutive models for materials rapidly solidifying from temperatures far above their melting point remains a major physical difficulty. Additionally, accurately defining the dynamic interface and modeling the transition from liquid spreading to solid contact, including its frictional, wetting, and bonding behavior, is inherently challenging for standard continuum-based FEM techniques, often necessitating complex and specialized numerical methods like VOF or Arbitrary Lagrangian–Eulerian frameworks.

4.3. Short Summary

A critical review of analytical formulations and numerical simulations for modeling residual stress evolution in individual splats has been provided. Analytical models based on classical thermoelasticity and simplified thermal mismatch assumptions offer quick estimations of average residual stress. However, these models cannot generally account for localized effects and stress relaxation mechanisms. In contrast, numerical simulations, particularly those employing FEM, SPH, and VOF approaches, enable detailed analysis of stress distributions and evolutions, considering elastic, plastic, and creep deformation during both the impact and cooling stages. Among these, multi-physics FEM models that incorporate temperature-dependent material properties, interface thermal contact resistance, and substrate compliance have demonstrated good agreement with experimental data, such as those obtained from FIB–DIC or strain gauge techniques. Across all models, higher substrate temperatures generally reduce residual tensile stress by facilitating gradual thermal contraction. Analytical models remain valuable for initial parameter screening and theoretical insight, whereas numerical simulations are essential for predictive modeling and optimizing process parameters. Future developments should prioritize integrating multiscale simulation frameworks, where individual splat behavior influences bulk coating performance, and advancing data-driven approaches, such as machine learning, to accelerate process optimization and enhance predictive accuracy.

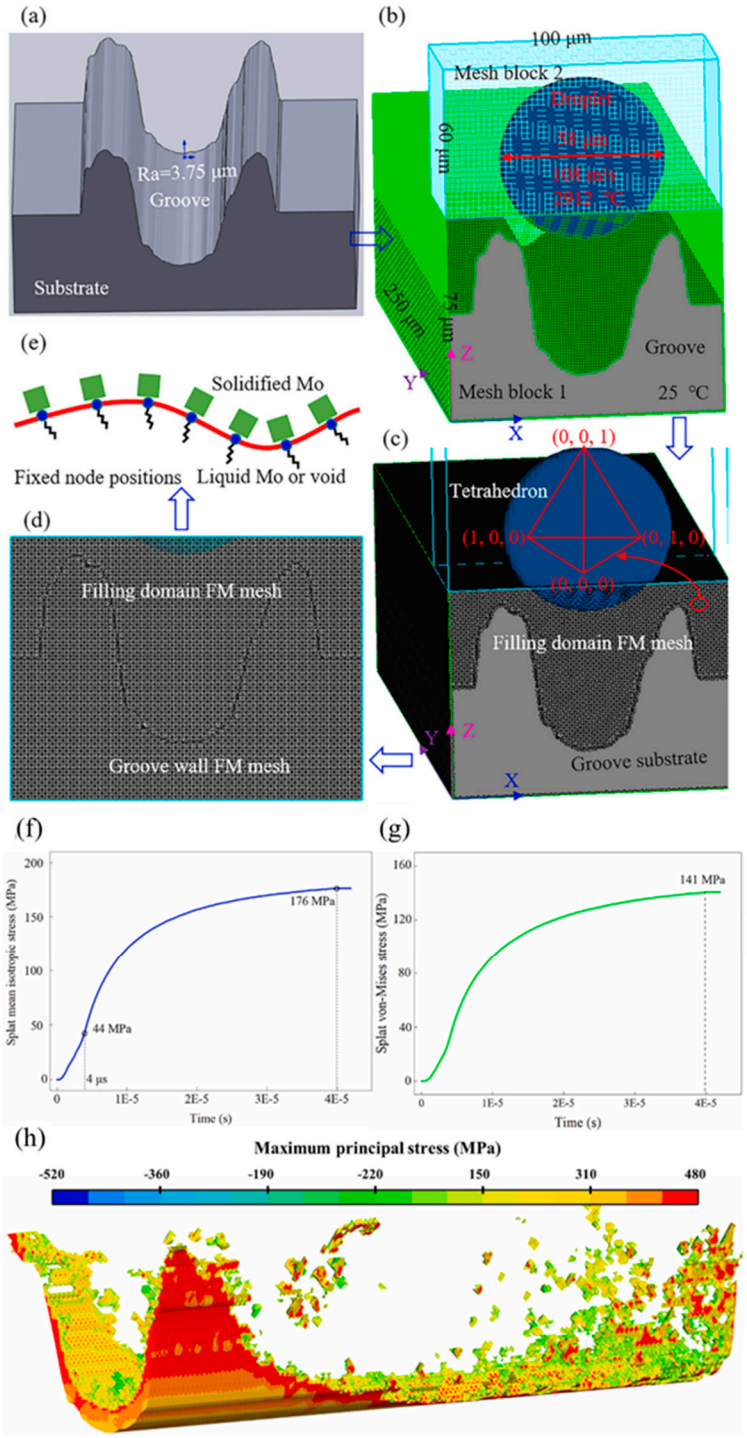

Figure 18. (**a**–**e**) Development process of a numerical model used for determining splat deposition stress during droplet impact on textured grooves. (**a**) Groove model. (**b**) Droplet impact simulation. (**c**,**d**) Mesh block 1 from the VOF method directly converted into a tetrahedral FEM model. (**e**) Established coupling relationship between the solidified and non-solidified states of the splat. (**f**–**h**) Mean isotropic stress, von Mises stress, and principal stresses in a splat: (**f**) time-varying mean isotropic stress, (**g**) time-varying von Mises stress, and (**h**) distribution of the maximum principal stress [79].

5. The Interplay of Bonding Strength and Residual Stress in Single Splats: Mechanisms and Control Strategies

5.1. Correlation Between Residual Stress and Interfacial Bonding Strength

The mechanical properties of a single splat are fundamentally affected by the processes occurring immediately upon impact: fluid dynamics, rapid heat transfer, and transient

solidification. The particle's impact velocity and temperature determine the extent of flattening and spreading, which directly influences the ultimate interfacial contact area and, consequently, the mechanical interlocking component of the bonding strength. Furthermore, the extremely high cooling rate (up to 10^8 K/s) that accompanies transient solidification governs the initial microstructural state and the formation of quenching residual stress. This transient solidification process is arguably the most critical step, as it determines the solid–liquid interfacial morphology, the degree of intimacy of contact, and the initial temperature boundary conditions that drive the subsequent thermal stress development.

In thermally sprayed coating systems, it is well known that residual stress can significantly affect measurements of interfacial bonding strength. Thouless et al. proposed that if residual stresses are relaxed during debonding, an additional contribution to the energy release rate is expected to influence the measurements [35]. Therefore, residual stresses should be considered to ensure the accurate interpretation of bonding strength measurements. Numerous studies have examined the effect of residual stress on the strain energy release rate of layered structures, particularly adhesively bonded joints [112–115]. A primary conclusion from these works is that the residual stress-induced energy release rate cannot be neglected when calculating the total energy release rate.

Tonshoff et al. investigated the effect of residual stress, introduced by pre-substrate treatment, on the interfacial bonding strength of sputtered PVD coatings during cutting machining [36]. They found that gradient compressive residual stress enhanced the adhesion strength and performance of coated cutting tools by compensating for high tensile loads during cutting processes. Yang et al. experimentally explored the effect of residual stress on the bonding strength of thermally sprayed hydroxyapatite coatings on Ti-6Al-4V substrates [37]. The residual stress and bonding strength were measured by XRD and tensile testing, respectively, with their correlation shown in Figure 19a. H1 (=25 °C), H2 (=160 °C), and H3 (=250 °C) denote various substrate temperatures. C1 (=air gas), C2 (=air/CO_2 mixed gas), and C3 (=no cooling gas) refer to various cooling media. It was demonstrated that coatings with higher compressive residual stress exhibited lower bonding strength, which was explained by the possibility that compressive stress could cause the coating to delaminate from the substrate. Godoy et al. examined the effect of coating thickness on bonding strength, observing a decrease with increasing thickness of NiCrAl coatings deposited on AISI 1020 substrates (Figure 19b) [116]. Their results suggested that the residual stress at the interface, rather than within the coating itself, influences interfacial bonding. Yang et al. also studied the effects of vacuum heat treatment on the residual stress and bonding strength of hydroxyapatite coatings thermally sprayed on Ti-6Al-4V alloy substrates [117]. They found that at a heating temperature of 500–600 °C, the compressive residual stress was released, thereby enhancing the bonding strength. However, at higher heating temperatures, the interfacial adhesion force was weakened by increased compressive residual strain. The compressive residual stress exhibits a crucial dual influence on splat integrity. The compressive stress is beneficial as it actively works to close Mode I (opening) cracks, effectively increasing the energy required for crack initiation and propagation. This mechanism fundamentally increases the fracture toughness of the interface. Additionally, high compressive stress is detrimental because it promotes a shift toward Mode II (sliding) or Mode III (tearing) loading at the interface, and critically, can lead to global splat delamination or buckling instability.

Nie et al. investigated the effect of residual stress on the energy release rate based on elasticity theory and FE analysis [118]. Their results demonstrate that the relationship between the energy release rate and residual stresses is governed by the system's critical buckling stress and cracked geometry, including the crack size and central deflection. Huang et al. investigated the effect of residual stress on the interfacial adhesion strength

of SiN thin films deposited on glass substrates by plasma-enhance chemical vapor deposition [119]. According to the nano-scratch tests, the interface adhesion energy decreased from 1.8 to 1.5 J/m^2 with decreasing residual compressive stress and increasing tensile stress. Residual compressive stress can dull crack tips and impede crack growth, while residual tensile stress can amplify the impact of applied shear stresses during scratch tests. This amplification enlarges the crack opening and thereby hastens fracture. Consequently, diminishing compressive stress or increasing tensile stress would accelerate interfacial failure and reduce the interface adhesion energy. Okajima et al. [120] employed a 2D FEM model to calculate the interfacial stress intensity factors (K_I) during tensile tests of ceramic coatings deposited on metal substrates, where a circumferential pre-crack was introduced at the periphery. In this model, residual stress was considered by comparing results with those from a specially designed model without a top coating. The results suggested that compressive residual stress within the coating promotes the closure of interfacial cracks, even without considering crack–surface contact. Therefore, the tensile stress near the crack tip negates the residual stress, causing a reduction in K_I. Conversely, compressive residual stress can intensify the tensile stress around the tip due to the reaction force generated by contact between the interfacial crack surfaces; consequently, the residual stress elevated K_I in this specific scenario.

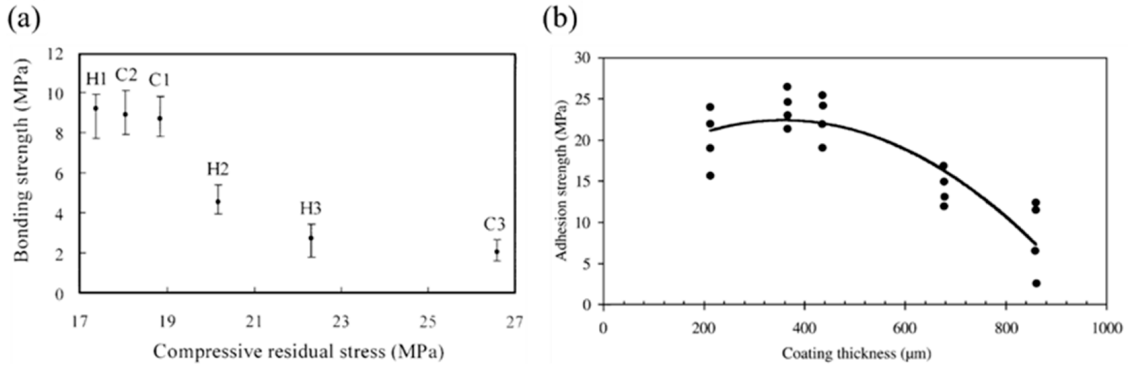

Figure 19. (**a**) Variation in bonding strength of the hydroxyapatite coatings with compressive residual stresses. H1 (=25 °C), H2 (=160 °C), and H3 (=250 °C) denote various substrate temperatures. C1 (=air gas), C2 (=air/CO_2 mixed gas), and C3 (=no cooling gas) refer to various cooling media [37]. (**b**) Adhesion strength of NiCrAl coatings deposited at different thicknesses on AISI 1020 substrates [116].

Few works have focused on situations involving single splats. The only relevant study was published in 2022 by Kang et al. [56], who experimentally investigated the effect of residual stress in a deposited paraffin wax splat, bonded with a stainless steel substrate, on the bonding shear strength, with particular consideration of the deposition conditions. Owing to the low melting point of the paraffin wax, the residual stress could be controlled by the self-stress relaxation process of the paraffin splat, which originates from creep deformation. During stress relaxation testing, approximately 70% of the tensile residual stress was released after the splat was held at 20 °C for 20 h [84]. By employing this method, the residual stress can be precisely controlled, becoming the only variable affecting bonding strength. Figure 20a plots the measured scraping forces and calculated $K(d)$ as a function of scraping distance, where $K(d)$ is a parameter indicating bonding strength (Equation (2)). Lower scraping forces and $K(d)$ were measured for higher residual stress. This is because the measured scraping force was partly relieved by the tensile residual stress, resulting in a lower measured scraping force and lower bonding strength for splats with high residual stress. The effect of droplet temperature at impact is shown in Figure 20b, where interfacial bonding increased with increasing droplet temperature for both low and

high residual stress conditions. This can be explained by stronger interfacial bonding at higher droplet temperatures [121,122].

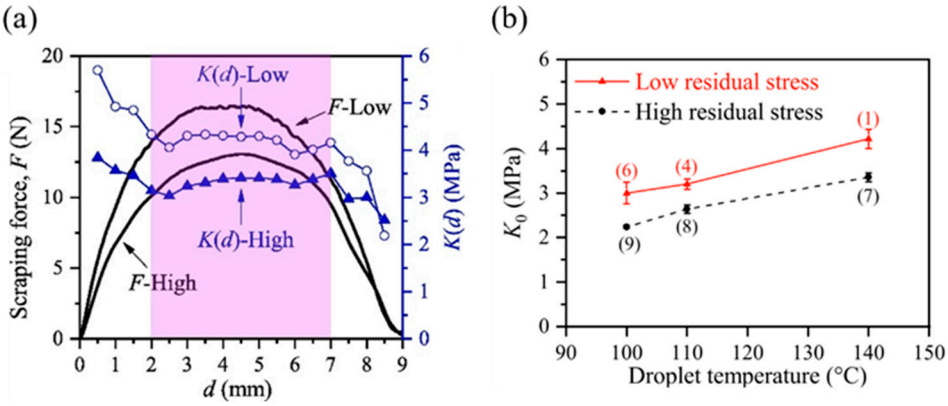

Figure 20. (**a**) Evolution of the scraping force and $K(d)$ versus scraping displacement in scraping tests. The curves illustrate the differences between low and high residual stress levels in the splats. (**b**) Maximum scraping forces (F_{max}) and calculated K_0 reveal the effects of droplet temperature and residual stress [56].

Nonetheless, predictive models that quantitatively link residual stress to interfacial bonding strength at the splat level have not been developed. Future work should address this while incorporating local stress fields, interfacial fracture mechanics, and contact phenomena. Additionally, identifying dominant stress components (e.g., interfacial shear, radial tensile, or compressive stresses) and their contributions to crack initiation and propagation is essential for building a mechanistic understanding of splat adhesion.

5.2. Factors Influencing Residual Stress of Single Splats

The evolution of residual stress in single splats is governed by a complex interplay of deposition parameters, material properties, and thermomechanical interactions during and after impact. Unlike macroscopic coatings, where stress distributions can be averaged over many layers, residual stress at the splat scale is highly localized and sensitive to transient conditions. Although important thermal spray variables, such as in-flight velocity and temperature, are often considered significant for coating properties, several studies have shown that their effect on the final residual stress in single splats is relatively limited under certain conditions [77,80], as illustrated in Figure 9a,b. Instead, the stress state is predominantly dictated by substrate preheating temperature, splat–substrate thermal mismatch, and post-deposition stress relaxation mechanisms.

Substrate preheating temperature is recognized as the dominant factor influencing the magnitude and sign of residual stress [104,106]. Residual stress in thermal spray splats is primarily composed of quenching stress and thermal stress. At low substrate temperatures, quenching stresses tend to dominate, often resulting in tensile residual stress due to the steep temperature gradient at the interface and rapid quenching [106]. As the substrate temperature increases, the contribution of thermal stress becomes more significant, and depending on the thermal expansion mismatch between the splat and substrate materials, the residual stress may shift from tensile to compressive [77,79,86]. For instance, in the case of ceramic splats deposited onto metal substrates, the lower thermal expansion coefficient of the ceramic results in compressive thermal stresses during cooling [80]. Combined experimental–numerical approaches have shown that interfacial stresses increase as the substrate temperature decreases, although these stresses can be partially relaxed by mechanisms such as interfacial debonding or microcracking [83].

Residual stress relaxation can occur via several mechanisms, which are fundamentally driven by thermodynamic and kinetic factors influenced by the splat's material behavior

and impact conditions. The process is driven by the system's inherent need to transform from a higher stored elastic strain energy state to a lower, more stable energy state. Mechanisms such as creep deformation [81,84,104] and plastic yielding [34] are kinetically and thermally activated. They rely on the motion of dislocations and other defects to convert elastic strain into permanent inelastic strain over time. For example, the rate of stress reduction is highly sensitive to both temperature and stress, which dictates the shift between dominant relaxation modes, such as the transformation from dislocation gliding to climbing as temperature exceeds a critical value. The stress reduction rate is reported to significantly increase as the stress exceeds the yielding strength or the temperature exceeds 170 °C for Al–Cu alloys [123]. Mechanisms like interfacial cracking [81,83] and edge curling [81,83,105] represent spontaneous stress relief. Cracking is especially prevalent in brittle ceramic splats, where microcracks can penetrate the surface and rapidly release local tensile stress near the crack tips. Edge curling, often observed in metallic splats, relieves through-thickness tensile stress by changing the splat's geometry to seek a lower total elastic energy state. In materials that undergo time-dependent deformation, such as amorphous or glassy ceramics, viscous flow above the glass transition temperature can lead to near-complete relaxation of quenching stress without any visible cracking [81]. For example, amorphous Al_2O_3–TiO_2–ZrO_2–CeO_2 splats showed considerable compressive residual stress due to this flow mechanism, in contrast to the partially relaxed tensile stress seen in polycrystalline Ni–Al splats, where yielding and edge curling dominate [81].

Numerical simulations have further elucidated the sensitivity of residual stress to interfacial thermal conductance. Fardan et al. [106] investigated the effect of varying thermal conductivity in YSZ splats using FEM modeling and found that although the general temporal and spatial patterns of stress distribution remained consistent, lower thermal conductance resulted in higher peak residual stresses. This highlights the importance of interfacial heat transfer efficiency, particularly in systems with thermal barriers or poorly bonded interfaces.

In summary, the residual stress state of single splats is primarily controlled by substrate preheating temperature and splat–substrate material properties, rather than by particle in-flight conditions. Understanding and optimizing these factors and accounting for relevant relaxation mechanisms are critical for minimizing stress-related defects, such as cracking, delamination, or curling up, and for ensuring reliable splat properties.

5.3. Strategies for Improving Interfacial Bonding

5.3.1. Optimizing the Substrate Preheating Temperature

Substrate preheating serves to remove adsorbates, condensates, and oxide layers, thereby fostering good interfacial wetting between the flattened particles and the underlying surface. This process facilitates the formation of disk-shaped splats, which possess advantageous interfacial adhesion characteristics [25,41,124,125]. Experiments have verified that coating adhesion strength changes with rising substrate temperature, and this dependency aligns with the observed splat morphology transition, as illustrated in Figure 21 [126]. Furthermore, when the preheat temperature surpasses the critical bonding point, the splat/substrate interface exhibits epitaxial growth combined with chemical metallurgical bonding [124]. However, excessive preheating negatively impacts the substrate's surface roughness and crystallographic properties, making it unsuitable for engineering thermal barrier coatings. Fukumoto et al. systematically investigated the effects of substrate temperature and ambient pressure on the flattening behaviors of several metallic splats thermally sprayed on polished metallic substrates [126]. They observed that the morphological shift from splash to disk splat occurred in most metallic systems by either reducing the ambient pressure or increasing the surface temperature. This indicates that the

desorption of surface contaminants independently drives the change in flattening behavior. The formation of disk-shaped and splashing deposits is primarily governed by five dimensionless parameters during particle impingement, based on a balance of inertia, viscous, and surface tension contributions [17]. High particle velocity induces finger-shaped splashing, a phenomenon closely related to the Weber and Ohnesorge numbers [127–129]. This rapid process, often accompanied by air entrapment, leads to the generation of a porous structure [130–132]. Crucially, the presence of strain and solidification immediately following impingement synergistically produces grain refinement and mechanical interlocking at the particle–substrate interface [44–46].

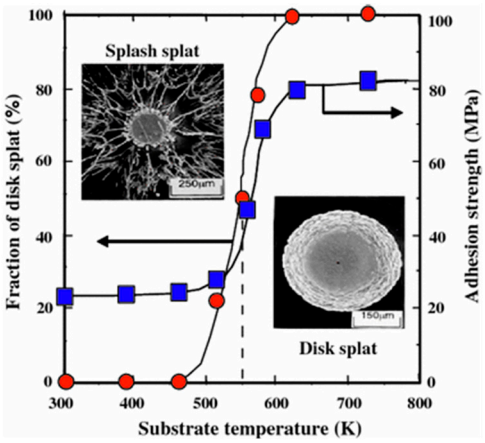

Figure 21. Dependence of the fraction of disk splats and coating adhesion strength on substrate temperature [126].

5.3.2. Improving Particle Impact Velocity

The influence of impact velocity on splashing and the resulting adhesion has been explained by Fauchais et al. using the Sommerfeld number (K) [21]. This takes place when K exceeds a critical threshold, which is calculated as follows:

$$K = \frac{\rho^2 d^2 v^{5/4}}{\gamma \eta} \tag{19}$$

where ρ is the density of the particle, d is its particle diameter, v is the mean particle velocity, γ is the dynamic viscosity, and η is the surface tension. As demonstrated in Figure 22, the morphology of the resulting splat gradually shifts from net-shaped to finger-shaped as the corresponding K value of the in-flight particles increases [55]. Early fluid dynamics studies predicted a critical threshold, K_c = 57.7, above which a droplet should splash. Experimentally, the correlation is more complex, where the splashing behavior in thermal spraying is not strictly governed by this theoretical value. Particles in typical thermal spray processes often have K values far exceeding this threshold, yet they still form well-adhered disk-shaped splats when the substrate is preheated. This critical deviation confirms that, for thermal spraying, the final splat morphology is a competition between the inertial forces (high Weber number) that promote splashing, and the extremely high-speed transient solidification that arrests the liquid spreading front. If solidification is fast enough, it suppresses the hydrodynamic instability that leads to splashing, forcing the morphology into a cohesive disk, regardless of a high Weber number or K value [133].

Focusing on low-velocity impact without splashing, Kang et al. experimentally studied the bonding strength and debonding behavior of a paraffin droplet deposited on a stainless-steel substrate, examining the effect of impact velocities [56]. The scraping results demonstrated that bonding strength improved as the impact velocity increased from 0.63 to 0.99 m/s. This finding showed some consistency with debonding behaviors, where

debonding was more likely to occur under a lower impact velocity. Wang et al. used nano-scratch tests to measure the bonding strength of supersonic or subsonic ceramic splats thermally sprayed on metal substrates [57]. Figure 23 presents the experimental results for subsonic and supersonic splats. As depicted in Figure 23a–d, subsonic splats were quickly peeled off the substrate following nano-scratch measurements. Based on statistical analysis, as shown in Figure 23e,f, the two experimental conditions revealed a similar trend for increasing and decreasing levels of adhesion. Compared with those of subsonic splats, the average adhesive force and shear strength of supersonic splats increased by 58% and 56%, respectively. Moreover, the adhesive force of the central region was approximately twice that of the peripheral region of splats (Figure 23e), which was mainly attributed to the formation of an air film.

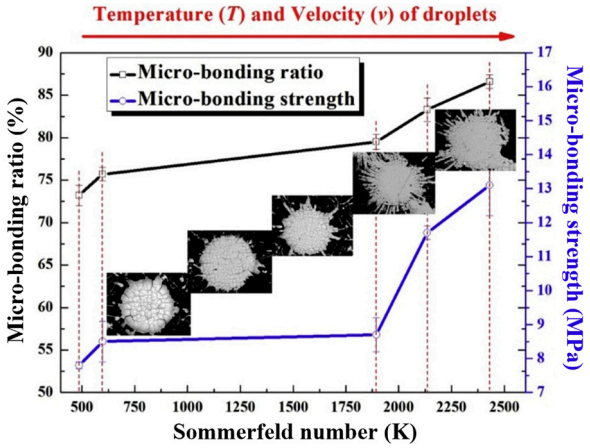

Figure 22. The relationship between the Sommerfeld number and splat–substrate micro-bonding properties [55].

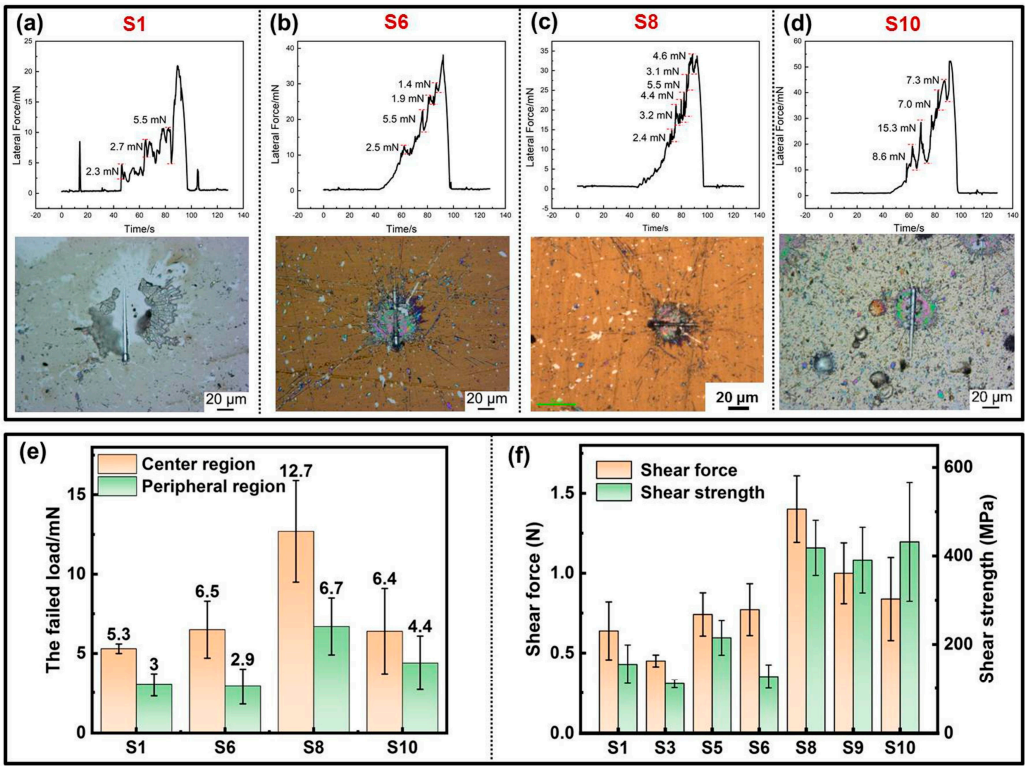

Figure 23. Nano-scratch curve and morphology of (**a**) S1, (**b**) S6, (**c**) S8, and (**d**) S10 splats. (**e**) Failure load corresponding to the detachment of the center region or the peripheral region from the substrate. (**f**) Shear force and strength of different splats. S1–S5 splats were subsonic, and S6–S10 were supersonic [57].

5.4. Role of Deposition Dynamics in Determining Mechanical Properties

To bridge the gap between initial process inputs and final mechanical outcomes, it is essential to explicitly correlate the transient fluid dynamics and thermal events to the resulting mechanical properties. Specifically, the fluid dynamics parameters govern the geometric extent of the bond by maximizing splat flattening and interfacial area, which directly enhances the mechanical interlocking component of bonding strength. Concurrently, the thermal parameters influence the quality and integrity of the bond by controlling interdiffusion, phase transformations, and the final magnitude and sign of the residual stress. Thus, the final reliability of the splat is a direct, coupled outcome of these initial fluid and thermal dynamics.

The deposition dynamics of single splats significantly influence their mechanical behaviors. Therefore, studying the flattening and solidification of deposited splats is expected to provide an in-depth understanding of the subsequent mechanical properties and performance of splats. It is known that deposition conditions, such as particle initial temperature [38], deposition velocity [39], substrate preheating temperature [40], and surface treatment [134], affect impact outcomes like spreading factors, splashing, fragmentation, and debonding. Many efforts have been made to optimize these deposition conditions and achieve desired splat properties. Notably, transient solidification at the splat/substrate interface plays a key role, not only in affecting spreading dynamics but also in dominating the interfacial microstructure, which directly influences the thermal and mechanical properties of coating systems [135–137]. This aspect deserves more attention and may further elucidate the factors regulating stress formation, especially during phase change and initial solidification. However, interfacial solidification has rarely been studied because of the experimental difficulties.

Recently, transparent substrates have been employed to observe interfacial phenomena during drop impact on a solid surface, with a special emphasis on gas traps [138], vapor films at the interface [139], and boiling [140]. Kang et al. thoroughly studied the impact dynamics and transient solidification of molten paraffin droplets on solid substrates [141,142]. Figure 24a illustrates the experimental setup used for assessing isothermal and non-isothermal impacts of a paraffin wax droplet on metal and transparent substrates. The change in geometry during impact was recorded using a high-speed camera (Figure 24b,c). Transparent substrates, including polycarbonate, quartz glass, and sapphire glass, were placed above a 45° tilted mirror for direct observation of the transient solidification at the interface. Figure 24d shows photographs of the bottom surface of impacted splats, where the splat contrast changed from black to white during solidification. The degree of interfacial solidification was quantified using the gray value: a greater gray value suggests a higher rate of solidification at the interface, and the splat is fully solidified at the interface when the gray value reaches a stable value. By comparing experimental results and numerical simulations, the gray values appear to be a good indicator for interfacial transient solidification. Furthermore, transient solidification significantly affects subsequent flattening behaviors, even though the solid layer is relatively thin, with a volume ratio of less than 2%.

Given that the fluid dynamics and mechanical aspects of splat formation have been bifurcated in the literature, a unified treatment remains elusive. Several studies have attempted to couple these aspects using separate models; for instance, fluid spreading and heat transfer are commonly modeled using finite volume methods or SPH, whereas stress development and cracking are handled using FEM. However, the distinct time scales and numerical constraints of these approaches pose substantial challenges for full integration. Overcoming these constraints is critical for developing predictive simulations that capture the complete splat evolution from impact dynamics to mechanical stabilization.

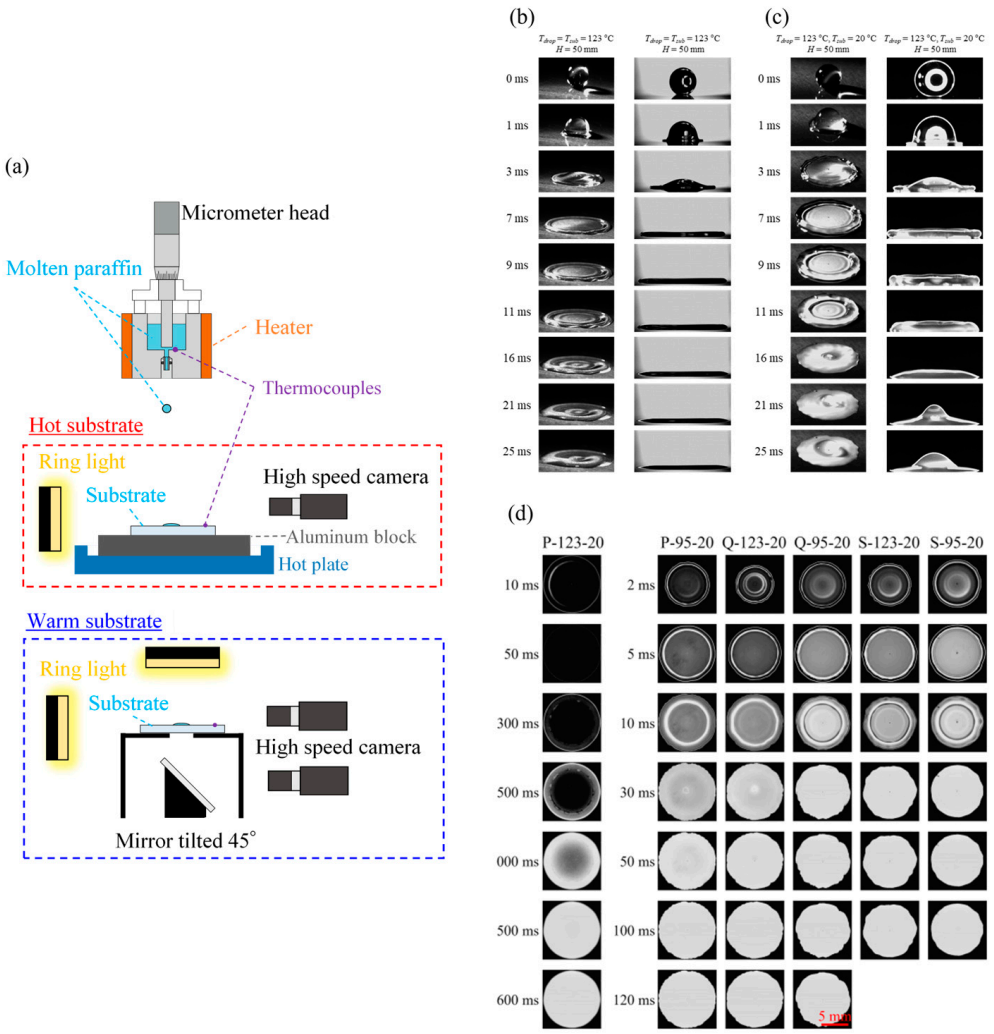

Figure 24. (**a**) Illustration of the setup used for droplet impact testing [142]. (**b**) Time-evolution of droplet impacts on an isothermal surface and (**c**) on a non-isothermal surface [141]. (**d**) Time-evolution of the splat–substrate interface, to quantify the transient solidification [142].

5.5. Short Summary

The interplay between two critical mechanical properties, namely bonding strength and residual stress, have been comprehensively reviewed in single splats. Compressive residual stresses may enhance or weaken bonding depending on the fracture mechanics, and tensile stresses generally reduce interfacial integrity by promoting crack opening and delamination. Regarding residual stress, the substrate preheating temperature is a crucial factor because it governs the balance between quenching and thermal stresses. Stress levels can also be partially relieved by relaxation mechanisms, including edge curling, microcracking, plastic yielding, and viscous or creep deformation, where the dominant mechanism depends on the splat's material behavior. Two primary approaches for improving bonding have been emphasized: increasing the substrate preheating temperature and optimizing the particle impact velocity. For practical applications, it is recommended that substrate temperature and particle velocity be jointly optimized to enhance bonding while minimizing residual stresses. Furthermore, future research should emphasize integrating process control with in situ diagnostics and multiscale modeling to guide material and process design for reliable and well-adhered splat formation. The complex interplay between deposition dynamics and mechanical properties in individual splats has also been highlighted. The transient solidification and spreading dynamics govern the initial contact conditions, which are foundational to mechanical outcomes. Predictive models that fully

capture this multi-physics problem—including fluid dynamics, heat transfer, phase change, and stress evolution—remain underdeveloped and warrant further development.

6. Summary and Perspective

6.1. Summary

This review covers the experimental methodologies and analytical models developed to investigate bonding strength and residual stress at the level of individual splats, focusing on the strategies for improving interfacial bonding and the factors influencing residual stress. Particular attention has been paid to the correlations between these two mechanical factors and how deposition dynamics influence the mechanical behavior of splats. The major conclusions are summarized as follows:

1. Characterization of bonding strength: Various techniques have been employed to measure the bonding strength at the splat/substrate interface. The scratch test remains the most widely applied owing to its relative simplicity and sensitivity to interfacial adhesion. However, more refined approaches, such as tensile loading, indentation, scraping, and FIB-milled microcantilever bending, have been used to capture interfacial fracture behavior under different loading modes. These studies collectively reveal that bonding strength is significantly influenced by particle impact velocity, substrate preheating, and interfacial solidification dynamics. Enhanced bonding typically results from higher kinetic energy, increased interfacial temperature, and improved chemical or metallurgical bonding during rapid solidification.
2. Measurement and modeling of residual stress: Residual stress in single splats arises from thermal contraction during solidification and quenching, as well as mismatched thermal expansion between the splat and substrate during subsequent cooling. Experimental methods, such as XRD, micro-indentation, and curvature measurements, have enabled residual stress quantification, but in situ techniques remain limited. FE simulations combined with thermal and mechanical modeling provide insight into transient stress evolution and distribution. These models have evolved to incorporate elastic, plastic, and time-dependent deformation mechanisms and increasingly use fluid dynamics outputs as initial conditions for mechanical simulations.
3. Coupling of bonding strength and residual stress: Bonding strength and residual stress are interrelated through their dependence on splat formation dynamics. Residual tensile stress can weaken the interface by partially offsetting externally applied stress during testing, thereby reducing apparent adhesion strength. Conversely, stress relaxation mechanisms, such as cracking, interfacial debonding, plastic yielding, and edge curling, may alter the stress state. As a result, the mechanical stability of a splat is not only a function of initial bonding but also of the stress evolution and dissipation during cooling.
4. Influence of deposition conditions: The mechanical outcomes of splats are governed by the interplay between particle velocity, temperature, substrate conditions, and material properties. Substrate preheating is particularly influential because it alters the cooling rate, quenching stress magnitude, and solidification front behavior. Furthermore, material-dependent properties, such as the thermal conductivity and CTE, control stress accumulation and relaxation behaviors across different splat–substrate systems.

6.2. Perspective

Although significant progress has been made in understanding the mechanical behavior of single splats, several fundamental challenges and opportunities for future research remain:

1. The mechanisms governing splat–substrate bonding and stress development are strongly influenced by transient phenomena during impact and solidification. How-

ever, real-time observation of interfacial phase changes, temperature gradients, and bonding formation remains largely inaccessible. The development of in situ detection techniques, such as high-speed imaging, high-speed thermal mapping, or electron microscopy with time-resolved capabilities, may provide unprecedented insight into interfacial processes at the sub-microsecond scale. This effort should be specifically prioritized for complex material systems like biomaterials and advanced ceramics.

2. Most current techniques for measuring bonding strength are either qualitative or subject to high variability because of the sample preparation and loading conditions. There is a critical need to establish standardized, reproducible methods for quantifying interfacial tensile and shear strength. This would not only improve comparability across studies but also enable more precise evaluation of the interfacial properties. Future research should aim to measure the true interfacial work of adhesion and to develop methods for high-frequency, time-resolved residual stress measurement.
3. Capturing the spatial and temporal evolution of residual stress during splat cooling remains a key issue. In situ methods, such as DIC and laser-based strain mapping, combined with advanced modeling that accounts for inelastic deformation and stress relaxation, are essential for the accurate prediction of residual stress states. Furthermore, modeling frameworks should include imperfect bonding, interfacial sliding, and phase-dependent mechanical properties.
4. A major gap in current computational approaches is the separation between fluid dynamics simulations (governing droplet spreading and solidification) and mechanical modeling (describing stress evolution). A unified multi-physics model that integrates hydrodynamics, heat transfer, phase transformation, and stress generation within a single simulation framework is highly desirable. Such a model is expected to enable the predictive design of deposition processes based on targeted mechanical outcomes at the splat scale, specifically by predicting outputs such as Cohesive Zone Model parameters and single-splat fracture toughness.

Author Contributions: Writing—original draft preparation, C.K.; writing—review and editing, C.K. and M.S.; project administration, M.S.; funding acquisition, M.S. All authors have read and agreed to the published version of the manuscript.

Funding: This work was supported by JSPS KAKENHI Grant-in-Aid for Scientific Research (B) 24K00755 and the Scientific Research Fund of Zhejiang Provincial Education Department (Y202456778).

Institutional Review Board Statement: Not applicable.

Informed Consent Statement: Not applicable.

Data Availability Statement: No new data were created or analyzed in this study.

Conflicts of Interest: The authors declare no conflict of interest.

References

1. Chandra, S.; Fauchais, P. Formation of solid splats during thermal spray deposition. *J. Therm. Spray Technol.* **2009**, *18*, 148–180. [CrossRef]
2. Berger, L.-M. Application of hardmetals as thermal spray coatings. *Int. J. Refract. Met. Hard Mater.* **2015**, *49*, 350–364. [CrossRef]
3. Li, C.-J.; Luo, X.T.; Yao, S.W.; Li, G.R.; Li, C.X.; Yang, G. The bonding formation during thermal spraying of ceramic coatings: A review. *J. Therm. Spray Technol.* **2022**, *31*, 780–817. [CrossRef]
4. Petrovicova, E.; Schadler, L.S. Thermal spraying of polymers. *Int. Mater. Rev.* **2002**, *47*, 169–190. [CrossRef]
5. Sathish, M.; Radhika, N.; Saleh, B. Duplex and composite coatings: A thematic review on thermal spray techniques and applications. *Met. Mater. Int.* **2023**, *29*, 1229–1297. [CrossRef]
6. Dorfman, M.R.; Dwivedi, G.; Dambra, C.; Wilson, S. Perspective: Challenges in the aerospace marketplace and growth opportunities for thermal spray. *J. Therm. Spray Technol.* **2022**, *31*, 672–684. [CrossRef]

7. Prashar, G.; Vasudev, H. Thermal sprayed composite coatings for biomedical implants: A brief review. *J. Therm. Spray Eng.* **2020**, *2*, 50–55. [CrossRef]
8. Kitamura, J.; Tang, Z.; Mizuno, H.; Sato, K.; Burgess, A. Structural, mechanical and erosion properties of yttrium oxide coatings by axial suspension plasma spraying for electronics applications. *J. Therm. Spray Technol.* **2011**, *20*, 170–185. [CrossRef]
9. Sampath, S. Thermal spray applications in electronics and sensors: Past, present, and future. *J. Therm. Spray Technol.* **2010**, *19*, 921–949. [CrossRef]
10. Von Niessen, K.; Gindrat, M. Plasma spray-PVD: A new thermal spray process to deposit out of the vapor phase. *J. Therm. Spray Technol.* **2011**, *20*, 736–743. [CrossRef]
11. Rodriguez, R.M.P.; Paredes, R.S.; Wido, S.H.; Calixto, A. Comparison of aluminum coatings deposited by flame spray and by electric arc spray. *Surf. Coat. Technol.* **2007**, *202*, 172–179. [CrossRef]
12. Picas, J.; Forn, A.; Matthäus, G. HVOF coatings as an alternative to hard chrome for pistons and valves. *Wear* **2006**, *261*, 477–484. [CrossRef]
13. Lett, S.; Quet, A.; Hémery, S.; Cormier, J.; Meillot, E.; Villechaise, P. Residual stresses development during cold spraying of Ti-6Al-4V combined with in situ shot peening. *J. Therm. Spray Technol.* **2023**, *32*, 1018–1032. [CrossRef]
14. Moridi, A.; Hassani-Gangaraj, S.M.; Vezzú, S.; Trško, L.; Guagliano, M. Fatigue behavior of cold spray coatings: The effect of conventional and severe shot peening as pre-/post-treatment. *Surf. Coat. Technol.* **2015**, *283*, 247–254. [CrossRef]
15. Rein, M. Phenomena of liquid drop impact on solid and liquid surfaces. *Fluid Dyn. Res.* **1993**, *12*, 61–93. [CrossRef]
16. Yarin, A.L. Drop impact dynamics: Splashing, spreading, receding, bouncing. . . *Annu. Rev. Fluid Mech.* **2006**, *38*, 159–192. [CrossRef]
17. Josserand, C.; Thoroddsen, S.T. Drop impact on a solid surface. *Annu. Rev. Fluid Mech.* **2016**, *48*, 365–391. [CrossRef]
18. Dykhuizen, R.C. Review of impact and solidification of molten thermal spray droplets. *J. Therm. Spray Technol.* **1994**, *3*, 351–361. [CrossRef]
19. Tiwari, A.; Samanta, R.; Chattopadhyay, H. Droplet solidification: Physics and modelling. *Appl. Therm. Eng.* **2023**, *228*, 120515. [CrossRef]
20. Cheng, X.; Sun, T.-P.; Gordillo, L. Drop impact dynamics: Impact force and stress distributions. *Annu. Rev. Fluid Mech.* **2022**, *54*, 57–81. [CrossRef]
21. Fauchais, P.; Fukumoto, M.; Vardelle, A.; Vardelle, M. Knowledge concerning splat formation: An invited review. *J. Therm. Spray Technol.* **2004**, *13*, 337–360. [CrossRef]
22. Li, L.; Vaidya, A.; Sampath, S.; Xiong, H.; Zheng, L. Particle characterization and splat formation of plasma sprayed zirconia. *J. Therm. Spray Technol.* **2006**, *15*, 97–105. [CrossRef]
23. Sobolev, V.V.; Guilemany, J.M. Flattening of droplets and formation of splats in thermal spraying: A review of recent work—Part 1. *J. Therm. Spray Technol.* **1999**, *8*, 87–101. [CrossRef]
24. Sobolev, V.V.; Guilemany, J.M. Flattening of droplets and formation of splats in thermal spraying: A review of recent work—Part 2. *J. Therm. Spray Technol.* **1999**, *8*, 301–314. [CrossRef]
25. Li, C.-J.; Yang, G.-J.; Li, C.-X. Development of particle interface bonding in thermal spray coatings: A review. *J. Therm. Spray Technol.* **2013**, *22*, 192–206. [CrossRef]
26. Kim, J. Spray cooling heat transfer: The state of the art. *Int. J. Heat Fluid Flow* **2007**, *28*, 753–767. [CrossRef]
27. Akhtar, S.; Xu, M.; Mohit, M.; Sasmito, A.P. A comprehensive review of modeling water solidification for droplet freezing applications. *Renew. Sustain. Energy Rev.* **2023**, *188*, 113768. [CrossRef]
28. Bolleddula, D.; Berchielli, A.; Aliseda, A. Impact of a heterogeneous liquid droplet on a dry surface: Application to the pharmaceutical industry. *Adv. Colloid Interface Sci.* **2010**, *159*, 144–159. [CrossRef]
29. Liang, G.; Mudawar, I. Review of drop impact on heated walls. *Int. J. Heat Mass Transf.* **2017**, *106*, 103–126. [CrossRef]
30. Khojasteh, D.; Kazerooni, M.; Salarian, S.; Kamali, R. Droplet impact on superhydrophobic surfaces: A review of recent developments. *J. Ind. Eng. Chem.* **2016**, *42*, 1–14. [CrossRef]
31. Shah, P.; Driscoll, M.M. Drop impact dynamics of complex fluids: A review. *Soft Matter* **2024**, *20*, 4839–4858. [CrossRef] [PubMed]
32. DelRio, F.W.; de Boer, M.P.; Knapp, J.A.; Reedy, E.D.; Clews, P.J.; Dunn, M.L. The role of van der Waals forces in adhesion of micromachined surfaces. *Nat. Mater.* **2005**, *4*, 629–634. [CrossRef]
33. Pawłowski, L. *The Science and Engineering of Thermal Spray Coatings*; John Wiley & Sons: Hoboken, NJ, USA, 2008.
34. Kuroda, S.C.T.W.; Clyne, T.W. The quenching stress in thermally sprayed coatings. *Thin Solid Film.* **1991**, *200*, 49–66. [CrossRef]
35. Thouless, M.; Jensen, H. The effect of residual stresses on adhesion measurements. *J. Adhes. Sci. Technol.* **1994**, *8*, 579–586. [CrossRef]
36. Tönshoff, H.K.; Seegers, H. Influence of residual stress gradients on the adhesion strength of sputtered hard coatings. *Thin Solid Film.* **2000**, *377*, 340–345. [CrossRef]
37. Yang, Y.-C.; Chang, E. Influence of residual stress on bonding strength and fracture of plasma-sprayed hydroxyapatite coatings on Ti–6Al–4V substrate. *Biomaterials* **2001**, *223*, 1827–1836. [CrossRef]
38. Sampath, S.; Jiang, X. Splat formation and microstructure development during plasma spraying: Deposition temperature effects. *Mater. Sci. Eng. A* **2001**, *304*, 144–150. [CrossRef]

39. Almohammadi, H.; Amirfazli, A. Droplet impact: Viscosity and wettability effects on splashing. *J. Colloid Interface Sci.* **2019**, *553*, 22–30. [CrossRef]
40. Paredes, R.S.C.; Amico, S.C.; d'Oliveira, A.S.C.M. The effect of roughness and pre-heating of the substrate on the morphology of aluminium coatings deposited by thermal spraying. *Surf. Coat. Technol.* **2006**, *200*, 3049–3055. [CrossRef]
41. Yang, G.-J.; Li, C.-X.; Hao, S.; Xing, Y.-Z.; Yang, E.-J.; Li, C.-J. Critical bonding temperature for the splat bonding formation during plasma spraying of ceramic materials. *Surf. Coat. Technol.* **2013**, *235*, 841–847. [CrossRef]
42. Hassani-Gangaraj, M.; Veysset, D.; Nelson, K.A.; Schuh, C.A. In-situ observations of single micro-particle impact bonding. *Scr. Mater.* **2018**, *145*, 9–13. [CrossRef]
43. He, P.-F.; Ma, G.-Z.; Wang, H.-D.; Tang, L.; Liu, M.; Bai, Y.; Wang, Y.; Tang, J.-J.; He, D.-Y.; Zhao, H.-C.; et al. Influence of in-flight particle characteristics and substrate temperature on the formation mechanisms of hypereutectic Al-Si-Cu coatings prepared by supersonic atmospheric plasma spraying. *J. Mater. Sci. Technol.* **2021**, *87*, 216–233. [CrossRef]
44. Liu, Z.; Wang, H.; Haché, M.; Irissou, E.; Zou, Y. Formation of refined grains below 10 nm in size and nanoscale interlocking in the particle–particle interfacial regions of cold sprayed pure aluminum. *Scr. Mater.* **2020**, *177*, 96–100. [CrossRef]
45. Reddy, C.D.; Zhang, Z.-Q.; Msolli, S.; Guo, J.; Sridhar, N. Impact induced metallurgical and mechanical interlocking in metals. *Comput. Mater. Sci.* **2021**, *192*, 110363. [CrossRef]
46. Jia, D.; Liu, Y.; Yi, P.; Zhan, X.; Ma, J.; Mostaghimi, J. Splat formation mechanism of droplet-filled cold-textured groove during plasma spraying. *Appl. Therm. Eng.* **2020**, *173*, 115239. [CrossRef]
47. Harfouche, M.M.; Alidokht, S.A.; Encalada, A.I.; Mungala, V.N.V.; Chromik, R.R.; Moreau, C.; Sharifi, N.; Stoyanov, P.; Makowiec, M.E. Scratch adhesion testing of thick HVOF thermal sprayed coatings. *J. Therm. Spray Technol.* **2024**, *33*, 1158–1166. [CrossRef]
48. Kromer, R.; Costil, S.; Verdy, C.; Gojon, S.; Liao, H. Laser surface texturing to enhance adhesion bond strength of spray coatings–Cold spraying, wire-arc spraying, and atmospheric plasma spraying. *Surf. Coat. Technol.* **2018**, *352*, 642–653. [CrossRef]
49. Wang, L.; Wang, Y.; Sun, X.; He, J.; Pan, Z.; Wang, C. Microstructure and indentation mechanical properties of plasma sprayed nano-bimodal and conventional ZrO_2–8wt% Y_2O_3 thermal barrier coatings. *Vacuum* **2012**, *86*, 1174–1185. [CrossRef]
50. Zhu, Q.; He, W.; Zhu, J.; Zhou, Y.; Chen, L. Investigation on interfacial fracture toughness of plasma-sprayed TBCs using a three-point bending method. *Surf. Coat. Technol.* **2018**, *353*, 75–83. [CrossRef]
51. Kaneko, K. Evaluation of the shearing strength of a WC-12Co thermal spray coating by the scraping test method. *Coatings* **2015**, *5*, 278–292. [CrossRef]
52. Dadvar, S.; Chandra, S.; Ashgriz, N. Adhesion of wax droplets to porous polymer surfaces. *J. Adhes.* **2015**, *91*, 538–555. [CrossRef]
53. Song, S.A.; Lee, C.K.; Bang, Y.H.; Kim, S.S. A novel coating method using zinc oxide nanorods to improve the interfacial shear strength between carbon fiber and a thermoplastic matrix. *Compos. Sci. Technol.* **2016**, *134*, 106–114. [CrossRef]
54. Kang, S.-K.; Lee, D.-B.; Choi, N.-S. Fiber/epoxy interfacial shear strength measured by the microdroplet test. *Compos. Sci. Technol.* **2009**, *69*, 245–251. [CrossRef]
55. Wang, Y.; Bai, Y.; Wu, K.; Zhou, J.; Shen, M.; Fan, W.; Chen, H.; Kang, Y.; Li, B. Flattening and solidification behavior of in-flight droplets in plasma spraying and micro/macro-bonding mechanisms. *J. Alloys Compd.* **2019**, *784*, 834–846. [CrossRef]
56. Kang, C.; Sakaguchi, M.; Saito, A.; Inoue, H. Adhesion strength of paraffin droplet impacted and solidified on metal substrate. *Results Phys.* **2022**, *34*, 105310. [CrossRef]
57. Wang, Y.; Bai, Y.; Yin, Y.; Wang, B.; Zheng, Q.; Yu, F.; Qin, Y.; Zhang, X.; Liu, M.; Wang, H. Wide-velocity range high-energy plasma sprayed yttria-stabilized zirconia thermal barrier coating—Part I: Splashing splat formation and micro-adhesive property. *Surf. Coat. Technol.* **2024**, *476*, 130280. [CrossRef]
58. Balić, E.E.; Hadad, M.; Bandyopadhyay, P.P.; Michler, J. Fundamentals of adhesion of thermal spray coatings: Adhesion of single splats. *Acta Mater.* **2009**, *579*, 5921–5926. [CrossRef]
59. Fanicchia, F.; Maeder, X.; Ast, J.; Taylor, A.; Guo, Y.; Polyakov, M.; Michler, J.; Axinte, D. Residual stress and adhesion of thermal spray coatings: Microscopic view by solidification and crystallisation analysis in the epitaxial CoNiCrAlY single splat. *Mater. Des.* **2018**, *153*, 36–46. [CrossRef]
60. Sabiruddin, K.; Bandyopadhyay, P.P. Scratch induced damage in alumina splats deposited on bond coats. *J. Mater. Process. Technol.* **2011**, *211*, 553–559. [CrossRef]
61. Keshri, A.K.; Debrupa, L.; Arvind, A. Carbon nanotubes improve the adhesion strength of a ceramic splat to the steel substrate. *Carbon* **2011**, *493*, 4340–4347. [CrossRef]
62. Jambagi, S.K.; Bandyopadhyay, P.P. Plasma sprayed carbon nanotube reinforced splats and coatings. *J. Eur. Ceram. Soc.* **2017**, *37*, 2235–2244. [CrossRef]
63. Pandey, K.K.; Shukla, D.K.; Verma, R.; Keshri, A.K. Mechanical property and adhesion strength of carbon nanofillers reinforced alumina single splats using in-situ picoindentation and nanoscratch test. *Ceram. Int.* **2021**, *479*, 26800–26807. [CrossRef]
64. Chen, S.-Y.; Ma, G.-Z.; Wang, H.-D.; He, P.-F.; Wang, H.-M.; Liu, M. Evaluation of adhesion strength between amorphous splat and substrate by micro scratch method. *Surf. Coat. Technol.* **2018**, *344*, 43–51. [CrossRef]

65. de Ruiter, J.; Oh, J.M.; van den Ende, D.; Mugele, F. Dynamics of collapse of air films in drop impact. *Phys. Rev. Lett.* **2012**, *108*, 074505. [CrossRef] [PubMed]
66. Turner, M.R.; Evans, A.G. An experimental study of the mechanisms of crack extension along an oxide/metal interface. *Acta Mater.* **1996**, *44*, 863–871. [CrossRef]
67. Matoy, K.; Schönherr, H.; Detzel, T.; Schöberl, T.; Pippan, R.; Motz, C.; Dehm, G. A comparative micro-cantilever study of the mechanical behavior of silicon based passivation films. *Thin Solid Film.* **2009**, *518*, 247–256. [CrossRef]
68. Chalker, P.R.; Bull, S.J.; Rickerby, D.S. A review of the methods for the evaluation of coating-substrate adhesion. *Mater. Sci. Eng. A* **1991**, *140*, 583–592. [CrossRef]
69. Chen, W.-P.; Chen, Y.-Y.; Huang, S.-H.; Lin, C.-P. Limitations of push-out test in bond strength measurement. *J. Endod.* **2013**, *39*, 283–287. [CrossRef]
70. Zhu, L.; Li, Y.; Chen, Y.-C.; Carrera, C.A.; Wu, C.; Fok, A. Comparison between two post-dentin bond strength measurement methods. *Sci. Rep.* **2018**, *8*, 2350. [CrossRef]
71. Salimijazi, H.R.; Raessi, M.; Mostaghimi, J.; Coyle, T. Study of solidification behavior and splat morphology of vacuum plasma sprayed Ti alloy by computational modeling and experimental results. *Surf. Coat. Technol.* **2007**, *2018*, 7924–7931. [CrossRef]
72. Fuse, J.; Yoshihara, Y.; Sano, M.; Inoue, F. Bond Strength Measurement for Wafer-Level and Chip-Level Hybrid Bonding. In Proceedings of the 2024 IEEE 10th Electronics System-Integration Technology Conference. (ESTC), Berlin, Germany, 11–13 September 2024; IEEE: Piscataway, NJ, USA, 2024.
73. Arai, M.; Eiji, W.; Kikuo, K. Residual stress analysis of ceramic thermal barrier coating based on thermal spray process. *J. Solid Mech. Mater. Eng.* **2007**, *10*, 1251–1261. [CrossRef]
74. Jing, F.; Yang, J.; Yang, Z.; Zeng, W. Critical compressive strain and interfacial damage evolution of EB-PVD thermal barrier coating. *Mater. Sci. Eng. A* **2020**, *776*, 139038. [CrossRef]
75. Mutter, M.; Mauer, G.; Mücke, R.; Guillon, O.; Vaßen, R. Correlation of splat morphologies with porosity and residual stress in plasma-sprayed YSZ coatings. *Surf. Coat. Technol.* **2017**, *318*, 157–169. [CrossRef]
76. Jiang, X.; Matejicek, J.; Sampath, S. Substrate temperature effects on the splat formation, microstructure development and properties of plasma sprayed coatings: Part II: Case study for molybdenum. *Mater. Sci. Eng. A* **1999**, *272*, 189–198. [CrossRef]
77. Matejicek, J.; Sampath, S. Intrinsic residual stresses in single splats produced by thermal spray processes. *Acta Mater.* **2001**, *491*, 1993–1999. [CrossRef]
78. Vaidya, A.; Streibl, T.; Li, L.; Sampath, S.; Kovarik, O.; Greenlaw, R. An integrated study of thermal spray process–structure–property correlations: A case study for plasma sprayed molybdenum coatings. *Mater. Sci. Eng. A* **2005**, *403*, 191–204. [CrossRef]
79. Jia, D.; Zhou, D.; Yi, P.; Zhang, C.; Li, J.; Guo, Y.; Zhang, S.; Li, Y. Splat deposition stress formation mechanism of droplets impacting onto texture. *Int. J. Mech. Sci.* **2024**, *266*, 109002. [CrossRef]
80. Das, B.; Pierre, B.; Partha, P.B. Raman spectroscopy assisted residual stress measurement of plasma sprayed and laser remelted zirconia splats and coatings. *Surf. Coat. Technol.* **2019**, *378*, 124920. [CrossRef]
81. Sebastiani, M.; Bolelli, G.; Lusvarghi, L.; Bandyopadhyay, P.; Bemporad, E. High resolution residual stress measurement on amorphous and crystalline plasma-sprayed single-splats. *Surf. Coat. Technol.* **2012**, *2063*, 4872–4880. [CrossRef]
82. Amano, A.; Sakaguchi, M.; Kurokawa, Y.; Okajima, Y.; Inoue, H. Measurement of quenching strain in paraffin drop test modelling thermal spray process. *Trans JSME* **2017**, *83*, 1–14.
83. Kang, C.; Sakaguchi, M.; Amano, A.; Kurokawa, Y.; Inoue, H. Quenching stress and fracture of paraffin droplet during solidification and adhesion on metallic substrate. *Surf. Coat. Technol.* **2019**, *374*, 868–877. [CrossRef]
84. Kang, C.; Sakaguchi, M.; Inoue, H. Contribution of creep to strain evolution in a paraffin droplet during and after rapid solidification on a metal substrate. *Surf. Coat. Technol.* **2020**, *399*, 126145. [CrossRef]
85. Matejicek, J.; Sampath, S.; Dubsky, J. X-ray residual stress measurement in metallic and ceramic plasma sprayed coatings. *J. Therm. Spray Technol.* **1998**, *7*, 489–496. [CrossRef]
86. Luo, Q.; Jones, A.H. High-precision determination of residual stress of polycrystalline coatings using optimised XRD-sin2ψ technique. *Surf. Coat. Technol.* **2010**, *205*, 1403–1408. [CrossRef]
87. Pope, C.G. X-ray diffraction and the Bragg equation. *J. Chem. Educ.* **1997**, *74*, 129. [CrossRef]
88. Teixeira, V.; Andritschky, M.; Fischer, W.; Buchkremer, H.; Stöver, D. Analysis of residual stresses in thermal barrier coatings. *J. Mater. Process. Technol.* **1999**, *92*, 209–216. [CrossRef]
89. Tsai, P.-C.; Hsu, C.-S. High temperature corrosion resistance and microstructural evaluation of laser-glazed plasma-sprayed zirconia/MCrAlY thermal barrier coatings. *Surf. Coat. Technol.* **2004**, *183*, 29–34. [CrossRef]
90. Korsunsky, A.M.; Sebastiani, M.; Bemporad, E. Focused ion beam ring drilling for residual stress evaluation. *Mater. Lett.* **2009**, *632*, 1961–1963. [CrossRef]
91. Korsunsky, A.M.; Sebastiani, M.; Bemporad, E. Residual stress evaluation at the micrometer scale: Analysis of thin coatings by FIB milling and digital image correlation. *Surf. Coat. Technol.* **2010**, *205*, 2393–2403. [CrossRef]

92. Sebastiani, M.; Eberl, C.; Bemporad, E.; Pharr, G.M. Depth-resolved residual stress analysis of thin coatings by a new FIB–DIC method. *Mater. Sci. Eng. A* **2011**, *5287*, 7901–7908. [CrossRef]
93. Wilkinson, A.J.; Meaden, G.; Dingley, D.J. High-resolution elastic strain measurement from electron backscatter diffraction patterns: New levels of sensitivity. *Ultramicroscopy* **2006**, *106*, 307–313. [CrossRef] [PubMed]
94. Arsenlis, A.; Parks, D. Crystallographic aspects of geometrically-necessary and statistically-stored dislocation density. *Acta Mater.* **1999**, *47*, 1597–1611. [CrossRef]
95. Nye, J.F. Some geometrical relations in dislocated crystals. *Acta Metall.* **1953**, *1*, 153–162. [CrossRef]
96. Kysar, J.W.; Saito, Y.; Oztop, M.; Lee, D.; Huh, W. Experimental lower bounds on geometrically necessary dislocation density. *Int. J. Plast.* **2010**, *26*, 1097–1123. [CrossRef]
97. Loginov, P.A.; Sidorenko, D.A.; Orekhov, A.S.; Levashov, E.A. A novel method for in situ TEM measurements of adhesion at the diamond–metal interface. *Sci. Rep.* **2021**, *11*, 10659. [CrossRef]
98. Loginov, P.A.; Fedotov, A.D.; Sheveyko, A.N.; Zaitsev, A.A.; Eganova, E.M.; Levashov, E.A. In Situ Heating TEM Study of the Interaction Between Diamond and Cu-Rich CoCrCuFeNi High-Entropy Alloy. *Metals* **2025**, *15*, 257. [CrossRef]
99. Zhou, R.; Sun, B.; Cai, H.; Li, C.; Pei, Y.; Gao, X.; Yang, K.; Shang, Y.; Zhao, X.; Li, S.; et al. High temperature in-situ synchrotron X-ray diffraction technique of thermal barrier coatings under thermal gradient and mechanical loads. *J. Mater. Res. Technol.* **2024**, *33*, 9155–9165.
100. Fernando, W.R.; Tantrigoda, D.; Rosa, S.; Jayasundara, D.R. Infrared thermography as a non-destructive testing method for adhesively bonded textile structures. *Infrared Phys. Technol.* **2019**, *98*, 89–93. [CrossRef]
101. Wen, B.; Zhou, Z.; Zeng, B.; Yang, C.; Fang, D.; Xu, Q.; Shao, Y.; Wan, C. Pulse-heating infrared thermography inspection of bonding defects on carbon fiber reinforced polymer composites. *Sci. Prog.* **2020**, *103*, 0036850420950131. [CrossRef]
102. Valente, T.; Bartuli, C.; Sebastiani, M.; Casadei, F. Finite element analysis of residual stress in plasma-sprayed ceramic coatings. *Proc. Inst. Mech. Eng. Part L J. Mater. Des. Appl.* **2004**, *218*, 321–330. [CrossRef]
103. Abubakar, A.A.; Arif, A.F.M. A hybrid computational approach for modeling thermal spray deposition. *Surf. Coat. Technol.* **2019**, *362*, 311–327. [CrossRef]
104. Chin, R.K.; Beuth, J.L.; Amon, C.H. Thermomechanical modeling of molten metal droplet solidification applied to layered manufacturing. *Mech. Mater.* **1996**, *24*, 257–271. [CrossRef]
105. Xue, M.; Chandra, S.; Mostaghimi, J. Investigation of splat curling up in thermal spray coatings. *J. Therm. Spray Technol.* **2006**, *15*, 531–536. [CrossRef]
106. Fardan, A.; Ahmed, R. Modeling the evolution of residual stresses in thermally sprayed YSZ coating on stainless steel substrate. *J. Therm. Spray Technol.* **2019**, *28*, 717–736. [CrossRef]
107. Abubakar, A.A.; Arif, A.F.M.; Akhtar, S.S.; Mostaghimi, J. Splats formation, interaction and residual stress evolution in thermal spray coating using a hybrid computational model. *J. Therm. Spray Technol.* **2019**, *28*, 359–377. [CrossRef]
108. Kamberov, G.; Kamberova, G.; Jain, A. 3D shape from unorganized 3D point clouds. In Proceedings of the International Symposium on Visual Computing, Lake Tahoe, NV, USA, 5–7 December 2005; Springer: Berlin/Heidelberg, Germany, 2005.
109. Garland, M.; Zhou, Y. Quadric-based simplification in any dimension. *ACM Trans. Graph.* **2005**, *24*, 209–239. [CrossRef]
110. Boyé, S.; Guennebaud, G.; Schlick, C. Least squares subdivision surfaces. In *Computer Graphics Forum*; Blackwell Publishing Ltd.: Oxford, UK, 2010; Volume 29.
111. Kazhdan, M.; Hoppe, H. Screened Poisson surface reconstruction. *ACM Trans. Graph.* **2013**, *32*, 29. [CrossRef]
112. Clyne, T.W.; Gill, S.C. Residual stresses in thermal spray coatings and their effect on interfacial adhesion: A review of recent work. *J. Therm. Spray Technol.* **1996**, *5*, 401–418. [CrossRef]
113. Nairn, J.A. On the calculation of energy release rates for cracked laminates with residual stresses. *Int. J. Fract.* **2006**, *139*, 267–293. [CrossRef]
114. Guo, S.; Dillard, D.A.; Nairn, J.A. Effect of residual stress on the energy release rate of wedge and DCB test specimens. *Int. J. Adhes. Adhes.* **2006**, *26*, 285–294. [CrossRef]
115. Shimamoto, K.; Sekiguchi, Y.; Sato, C. The critical energy release rate of welded joints between fiber-reinforced thermoplastics and metals when thermal re-sidual stress is considered. *J. Adhes.* **2016**, *92*, 306–318. [CrossRef]
116. Godoy, C.; Souza, E.A.; Lima, M.M.; Batista, J.C.A. Correlation between residual stresses and adhesion of plasma sprayed coatings: Effects of a post-annealing treatment. *Thin Solid Film.* **2002**, *420*, 438–445. [CrossRef]
117. Yang, Y.-C. Influence of residual stress on bonding strength of the plasma-sprayed hydroxyapatite coating after the vacuum heat treatment. *Surf. Coat. Technol.* **2007**, *201*, 7187–7193. [CrossRef]
118. Nie, P.; Shen, Y.; Chen, Q.; Cai, X. Effects of residual stresses on interfacial adhesion measurement. *Mech. Mater.* **2009**, *41*, 545–552. [CrossRef]
119. Huang, Y.-C.; Chang, S.-Y.; Chang, C.-H. Effect of residual stresses on mechanical properties and interface adhesion strength of SiN thin films. *Thin Solid Film.* **2009**, *5177*, 4857–4861. [CrossRef]

120. Okajima, Y.; Sakaguchi, M.; Inoue, H. A finite element assessment of influential factors in evaluating interfacial fracture toughness of thermal barrier coating. *Surf. Coat. Technol.* **2017**, *313*, 184–190. [CrossRef]
121. Yao, S.-W.; Li, C.-J.; Tian, J.-J.; Yang, G.-J.; Li, C.-X. Conditions and mechanisms for the bonding of a molten ceramic droplet to a substrate after high-speed impact. *Acta Mater.* **2016**, *119*, 9–25. [CrossRef]
122. Chao, Y.-P.; Qi, L.-H.; Zuo, H.-S.; Luo, J.; Hou, X.-H.; Li, H.-J. Remelting and bonding of deposited aluminum alloy droplets under different droplet and substrate temperatures in metal droplet deposition manufacture. *Int. J. Mach. Tools Manuf.* **2013**, *69*, 38–47. [CrossRef]
123. Song, H.; Gao, H.; Zhang, Q.; Zhou, X.; Zhang, B. Long-term stress relaxation behaviors and mechanisms of 2219 Al–Cu alloy under various temperatures and initial stresses. *J. Mater. Sci. Technol.* **2024**, *180*, 174–192. [CrossRef]
124. Yao, S.-W.; Liu, T.; Li, C.-J.; Yang, G.-J.; Li, C.-X. Epitaxial growth during the rapid solidification of plasma-sprayed molten TiO_2 splat. *Acta Mater.* **2017**, *134*, 66–80. [CrossRef]
125. Sampath, S.; Jiang, X.; Matejicek, J.; Leger, A.; Vardelle, A. Substrate temperature effects on splat formation, microstructure development and properties of plasma sprayed coatings Part I: Case study for partially stabilized zirconia. *Mater. Sci. Eng. A* **1999**, *272*, 181–188. [CrossRef]
126. Fukumoto, M.; Yamaguchi, T.; Yamada, M.; Yasui, T. Splash splat to disk splat transition behavior in plasma-sprayed metallic materials. *J. Therm. Spray Technol.* **2007**, *16*, 905–912. [CrossRef]
127. Duan, R.-Q.; Koshizuka, S.; Oka, Y. Two-dimensional simulation of drop deformation and breakup at around the critical Weber number. *Nucl. Eng. Des.* **2003**, *225*, 37–48. [CrossRef]
128. Xiao, F.; Dianat, M.; McGuirk, J. A robust interface method for drop formation and breakup simulation at high density ratio using an extrapolated liquid velocity. *Comput. Fluids* **2016**, *136*, 402–420. [CrossRef]
129. Nykteri, G.; Gavaises, M. Droplet aerobreakup under the shear-induced entrainment regime using a multiscale two-fluid approach. *Phys. Rev. Fluids* **2021**, *6*, 084304. [CrossRef]
130. Shukla, R.K.; Kumar, A.; Kumar, R.; Singh, D.; Kumar, A. Numerical study of pore formation in thermal spray coating process by investigating dynamics of air entrapment. *Surf. Coat. Technol.* **2019**, *378*, 124972. [CrossRef]
131. Li, D.; Zhang, D.; Zheng, Z.; Tian, X. Numerical analysis on air entrapment during a droplet impacts on a dry flat surface. *Int. J. Heat Mass Transf.* **2017**, *115*, 186–193. [CrossRef]
132. Qu, M.; Wu, Y.; Srinivasan, V.; Gouldstone, A. Observations of nanoporous foam arising from impact and rapid solidification of molten Ni droplets. *Appl. Phys. Lett.* **2007**, *90*, 254101. [CrossRef]
133. Yang, K.; Liu, M.; Zhou, K.; Deng, C. Recent developments in the research of splat formation process in thermal spraying. *J. Mater.* **2013**, *2013*, 260758. [CrossRef]
134. Tran, A.T.T.; Hyland, M.; Qiu, T.; Withy, B.; James, B. Effects of surface chemistry on splat formation during plasma spraying. *J. Therm. Spray Technol.* **2008**, *17*, 637–645. [CrossRef]
135. Xing, Y.-Z.; Liu, Z.; Wang, G.; Li, X.-H.; Jiang, C.-P.; Chen, Y.-N.; Zhang, Y.; Song, X.-D.; Dargusch, M. Improvement of interfacial bonding between plasma-sprayed cast iron splat and aluminum substrate through preheating substrate. *Surf. Coat. Technol.* **2017**, *316*, 190–198. [CrossRef]
136. Wang, J.; Luo, X.-T.; Li, C.-J.; Ma, N.; Takahashi, M. Effect of substrate temperature on the microstructure and interface bonding formation of plasma sprayed Ni20Cr splat. *Surf. Coat. Technol.* **2019**, *371*, 36–46. [CrossRef]
137. Guo, L.; Zhang, Y.; Wang, F.; Xin, Z.; Wang, G.; Jiang, J. Interface structure, mechanics and corrosion resistance of nano-ceramic composite coated steels. *Appl. Surf. Sci.* **2024**, *669*, 160525. [CrossRef]
138. Chantelot, P.; Lohse, D. Drop impact on superheated surfaces: From capillary dominance to nonlinear advection dominance. *J. Fluid Mech.* **2023**, *963*, A2. [CrossRef]
139. Castanet, G.; Chaze, W.; Caballina, O.; Collignon, R.; Lemoine, F. Transient evolution of the heat transfer and the vapor film thickness at the drop impact in the regime of film boiling. *Phys. Fluids* **2018**, *30*, 122109. [CrossRef]
140. Tran, T.; Staat, H.J.J.; Prosperetti, A.; Sun, C.; Lohse, D. Drop impact on superheated surfaces. *Phys. Rev. Lett.* **2012**, *108*, 036101. [CrossRef]
141. Kang, C.; Ikeda, I.; Sakaguchi, M. Recoil and solidification of a paraffin droplet impacted on a metal substrate: Numerical study and experimental verification. *J. Fluids Struct.* **2023**, *118*, 103839. [CrossRef]
142. Kang, C.; Ikeda, I.; Sakaguchi, M. Spreading dynamics associated with transient solidification of a paraffin droplet impacting a solid surface. *Int. J. Heat Mass Transf.* **2024**, *228*, 125672. [CrossRef]

Disclaimer/Publisher's Note: The statements, opinions and data contained in all publications are solely those of the individual author(s) and contributor(s) and not of MDPI and/or the editor(s). MDPI and/or the editor(s) disclaim responsibility for any injury to people or property resulting from any ideas, methods, instructions or products referred to in the content.